2015

# Temperature-dependent thermal and electrical conduction in metallic nanostructures

Zhe Cheng
*Iowa State University*

**Temperature-dependent thermal and electrical conduction in metallic nanostructures**

by

**Zhe Cheng**

A thesis submitted to the graduate faculty

in partial fulfillment of the requirements for the degree of

MASTER OF SCIENCE

Major: Mechanical Engineering

Program of Study Committee:
Xinwei Wang, Major Professor
Meng Lu
Chenxu Yu

Iowa State University

Ames, Iowa

2015

# TABLE OF CONTENTS

Page

# LIST OF FIGURES

Page

# LIST OF TABLES

# ACKNOWLEDGMENTS

Time flies so fast that I even don't notice that I have stayed in Ames for about two years. I believe this period of time would play an important role in my life. The first one I want to express my gratitude to is my major professor and academic advisor, Dr. Xinwei Wang. He taught me how to design experiments, how to solve problems encountered in experiments, how to write academic paper and how to analyze, extract the physical mechanism behind the experiment phenomena. Without his support, patience and guidance, I can never finish this degree. Special thanks to him for giving me the freedom to direct my research to what I am interested.

I would like to thank the members of my committee, Dr. Meng Lu and Dr. Chenxu Yu. Especially, I want to thank Dr. Lu and Longju Liu for their help in the silver nanowire project. In the two years, I learned a lot from my lab-mates in the Micro/Nanoscale Thermal Science Laboratory: Zaoli Xu, Shen Xu, Huan Lin, Chong Li, Jing Liu, Yangsu Xie, Chris Reilly, Pengyu Yuan, Meng Han, Bowen Zhu, Tianyu Wang. I am grateful for their help in both life and study. I wish the best of luck to all of them in their future endeavors. Also, I want to thank all my friends in Ames.

I would like to thank my parents for their unconditional love, support and encouragement which make it possible for me to pursue my dream!

# ABSTRACT

In this work, temperature dependent electrical and thermal conduction in the bio-supported 3.2 nm-thin Ir nanofilm and individual silver nanowire are studied at reduced temperatures. For the Ir film, by studying the temperature-dependent behavior (300 K down to 43 K) of electron thermal conductivity ($\kappa$), we quantify the extremely confined defect-electron scatterings and isolate the intrinsic phonon-electron scattering that is shared by the bulk Ir. At low temperatures below 50 K, $\kappa$ of the film has almost two orders of magnitude reduction from that of bulk Ir. The film has $\partial\kappa/\partial T>0$ while the bulk Ir has $\partial\kappa/\partial T<0$. We introduce a unified thermal resistivity ($\Theta=T/\kappa$) to interpret these completely different $\kappa\sim T$ relations. It is found that the film and the bulk Ir share a very similar $\Theta\sim T$ trend while they have a different residual part ($\Theta_0$) at 0 K limit: $\Theta_0\sim0$ for the bulk Ir, and $\Theta_0=5.5$ m·K$^2$/W for the film. The Ir film and the bulk Ir have very close $\partial\Theta/\partial T$ (75 to 290 K): $6.33\times10^{-3}$ mK/W for the film and $7.62\times10^{-3}$ mK/W for the bulk Ir. This strongly confirms the similar phonon-electron scattering in them. The temperature dependent behavior of the Lorenz number of the Ir film is also reported down to 10 K. Due to the strong defect-electron scattering, a very large residual electrical resistivity ($1.24\times10^{-7}$ Ω·m) is observed for the film that dominates the overall electron transport ($1.24\sim1.55\times10^{-7}$ Ω·m). The Debye temperature (221 K) of the film is found much smaller than that of bulk (308 K). This phonon softening strongly confirms the extensive surface and grain boundary electron scatterings. We find the Wiedemann-Franz Law still applies to our film even at low temperatures. The overall Lorenz number and that of imperfect structure ($\sim2.25\times10^{-8}$ W·Ω/K$^2$) are close to the Sommerfeld value and shows little temperature dependence. This is contrast to other studied low dimensional metallic structures that have a much larger Lorenz

number ($3\sim7\times10^{-8}$ $W\cdot\Omega/K^2$). Electron tunneling and hopping in the biomaterial substrate are speculated responsible for the observed Lorenz number.

Additionally, the thermal and electrical transport in an individual silver nanowire is characterized down to 35 K for in-depth understanding of the strong structural defect induced electron scattering. The results indicate that, at room temperature, the electrical resistivity increases by around 4 folds from that of bulk silver. The Debye temperature (151 K) of the silver nanowire is found 36% lower than that (235 K) of bulk silver, confirming strong phonon softening. At room temperature, the thermal conductivity is reduced by 55% from that of bulk silver. This reduction becomes larger as the temperature goes down. A large residual $\Theta$ is observed for silver nanowire while that of the bulk silver is almost zero. The same $\Theta \sim T$ trend proposes that the silver nanowire and bulk silver share the similar phonon-electron scattering mechanism for thermal transport. Due to phonon-assisted electron energy transfer across grain boundaries, the Lorenz number of the silver nanowire is found much larger than that of bulk silver and decreases with decreasing temperature.

# CHAPTER 1
# INTRODUCTION

## 1.1 Metallic Nanofilm

Metallic ultra-thin films are widely used as interconnects in the microelectronics and play an important role in related thermal design in micro/nanoscale devices and systems.[7] The device performance in these applications is significantly affected by the energy transport and dissipation in the metallic films. These films are composed of nanocrystals and electron dominates in their thermal transport. When the film dimension is either comparable to or less than the electron mean free path, the grain boundaries and surfaces scatter electrons strongly.[8, 9] As a result, the thermal properties of metallic ultra-thin films behave very differently from their bulk counterparts, especially at low temperatures when the phonon-electron scattering diminishes gradually. The thinner the film thickness is, the stronger grain boundary and surface scatterings are. Subsequently, the thermal behavior difference between the film and their bulk counterpart becomes larger. Data for these extremely confined domains will be in high demand in the future applications. However, due to the difficulties in accurate in-plane thermal conductivity characterization of nanometer-thick metallic films at low temperatures, few experimental results are available. Yoneoka *et al.* measured thermal conductivity of platinum films with a thickness of 7.3, 9.8, and 12.1 nm from 320 K to 50 K. The authors used the 3-Omega method to measure the thermal conductivity of the Pt film. Its measurement error is 9%-17%.[10] Zhang and co-workers investigated the thermal transport in 53 nm and 76 nm thick Au nanofilms from 300 K to 3 K and 48 nm thick platinum nanofilms from 300 K to 60 K using a direct current heating method. The authors did not estimate the accuracy but the accuracy of the

thermal conductivity depends on that of many other parameters, like the temperature coefficient of resistance and the geometry of the sample. The error of these parameters would accumulate when calculating the thermal conductivity.[11, 12] It is noticeable that the thinnest metallic film whose temperature dependent thermal conductivity has been measured so far is the 7.3 nm platinum film studied by Yoneoka and coworkers. For extremely thin films (sub-5 nm thick), the temperature dependent nature of thermal conductivity has not been studied before, even though such work is crucial for understanding of electron thermal transport with extremely strong defect scatterings at low temperatures. Therefore, it is of great importance to extend the thickness limit and an in-depth study of energy dissipation and transport in the sub-5 nm regime is overdue.

## 1.2 Metallic Nanowire

Metallic nanowires, especially silver nanowires, have attracted considerable attention recently due to its great potentials for applications like flexible touch screen, solar cells and transparent electrodes.[13-17] For the design and optimization of these applications, the thermal and electrical properties of an individual nanowire are critical and fundamental but they have been rarely reported. Up to now, the electrical properties of nanowires, especially inert metallic nanowires and nanowire bundles, are not difficult to measure.[18-21] But for thermal property characterization, only a few experimental investigations have been reported due to the difficulties in suspending a single nanowire, reducing contact resistance and accurate thermal measurement. Ou *et al.* investigated the thermal and electrical conductivities of a single nickel nanowire from 15 K to 300 K. Its Lorenz number is larger than Sommerfeld value with temperature above 75 K and decreased rapidly when the temperature goes below 75 K.[22] The experimental results of Völklein *et al.* showed the thermal and electrical conductivities of a

single Pt nanowire from 260 K to 360 K. The Lorenz number was smaller than the Sommerfeld value while the reasons are unclear in their work. [23] Stojanovic *et al.* measured the thermal conductivity of aluminum nanowire arrays instead of a single nanowire at room temperature. The thermal conductivity of these nanowire arrays is measured as 105-145 W/K·m when the widths of the nanowires ranged from 75 nm to 150 nm. The phonon contribution to the total thermal conductivity is about 21 W/K·m.[24] For a single silver nanowire, it has not been studied before even though it is of great importance to understand its electrical and thermal properties.

## 1.3 Lorenz Number of Nanostructures

For most bulk metals, the ratio of thermal and electrical conductivity at a certain temperature is a constant, namely Lorenz number, which is well-known as the Wiedemann-Franz (WF) Law. The Lorenz number of bulk metals is temperature dependent. Its value equals the Sommerfeld value ($2.44\times10^{-8}$ W·Ω/K$^2$) at high temperatures (above Debye temperature) and extreme low temperatures (a few Kelvins). For intermediate temperatures, the Lorenz number decreases with decreasing temperature.[25] But for nanocrystalline metallic films, the WF law has been reported to be violated due to grain boundary-electron reflection and electron-phonon scattering.[10, 26] When the grain size of nanocrystalline metallic films is either comparable to or less than the electron mean free path, the grain boundary-electron and surface-electron scatterings are intensive. The energy of scattered electrons can be partly transferred across the grain boundary via electron-phonon scattering because phonons can transport through the grain boundary more readily than electrons. This results in the evidently reduced electrical conductivity and less reduced thermal conductivity. Consequently, the Lorenz numbers of nanocrystalline metallic films are larger than the Sommerfeld value. Furthermore, the trend of

nanocrystalline metallic films' Lorenz number versus temperature also behaves quite differently from that of bulk materials due to the difference in scattering mechanism.[23, 27] These differences make it an interesting and important topic to investigate the mechanism of electrical and thermal transport in metallic nanofilms.

However, due to the difficulties in sample preparation and in-plane thermal conductivity characterization of nanometer-thick metallic films, especially for less than 5 nm thick films, only a few experimental measurements have been reported. Yoneoka *et al.* measured the electrical and thermal conductivity of platinum films with a thickness of 7.3, 9.8, and 12.1 nm from 320 K to 50 K. They obtained average Lorenz numbers as $3.82\times10^{-8}$, $2.79\times10^{-8}$, and $2.99\times10^{-8}$ $W\cdot\Omega/K^2$ respectively.[10] Zhang and co-workers investigated the electrical and thermal transport in 53 nm and 76 nm thick Au nanofilms from 300 K to 3 K. They found that the Lorenz numbers were about $4\times10^{-8}$ and $3.5\times10^{-8}$ $W\cdot\Omega/K^2$ respectively and showed weak temperature dependence from 300 K to 40 K. When the temperature went below 40 K, the Lorenz number increased notably with decreasing temperature.[11] Zhang and co-workers did similar work on 48 nm thick platinum nanofilms from 300 K to 60 K. Their experimental results showed that the Lorenz number was about three times larger than the bulk counterpart near room temperature and increased slowly with decreasing temperature.[12] Wilson *et al.* experimentally confirmed that the Wiedemann-Franz Law was valid for nanoscale Pd/Ir interfaces.[28]

## 1.4 Our Work

In this work, a robust and accurate technique developed in our lab [26, 29] named transient electro-thermal (TET) technique, is used to characterize the electrical and thermal transport in ultra-thin metallic films simultaneously and determine the Lorenz number precisely.

The studied nanocrystalline Iridium (Ir) films have an average thickness of 3.2 nm and are studied from 300 K to 43 K. The temperature dependence of thermal conductivity is investigated and compared with that of bulk Ir to reveal the extremely strong structural scattering effect. A unified thermal resistivity is introduced to interpret the completely different thermal conductivity variation trends against temperature for the film and bulk Ir. The electrical properties of the 3.2 nm-thin nanocrystalline Ir films on milkweed floss are measured from 290 K to 10 K and the phonon softening phenomenon is observed. The temperature dependence of the Lorenz number is also investigated and the Lorenz number of the structural imperfection is defined and evaluated. Additionally, the electrical conductivity and Lorenz number is compared with that of bulk Ir respectively to reveal the strong structural scattering.

For individual silver nanowire, it is suspended across two electrodes and Electron Beam Induced Deposition (EBID) is used to deposit Pt pads on the ends of the nanowire to suppress the electrical and thermal contact resistances. The thermal and electrical properties of the single suspended silver nanowire are characterized with a steady-state electro-thermal technique from room temperature down to 35 K. The temperature dependent Lorenz number is also determined. The thermal and electrical conductivities of the nanowire are compared with their bulk counterpart to reveal the nanowire's structure-property relation and unified thermal resistivity is used to reveal the scattering mechanism.

# CHAPTER 2
# ELECTRICAL AND THERMAL TRANSPORT IN METALLIC NANOFILM

## 2.1. Sample Structure

The ultra-thin Ir films studied in this work cannot support themselves due to its very fine thickness. Therefore, milkweed floss is selected as the substrate to support the ultra-thin Ir films for reasons given later. The milkweed floss is collected from a dry milkweed seed pod grown in Ames, Iowa, USA. The milkweed seeds and floss are shown in figure 1(a). Figure 1(b) depicts the SEM image of a single milkweed fiber suspended across two electrodes. The two ends of the fiber are long enough to avoid being embedded in the silver paste. This ensures that the silver paste will not enter the hollow part of the fiber. The inset shows the smooth floss surface. Figure 1(c) depicts the SEM image of the milkweed fiber cross section. The definition of the maximum Ir film thickness $\delta_{\max}$, diameter $d$ and cell wall thickness $\delta_{floss}$ are shown in figure 1(d). The average thickness of Ir films is $\delta_{ave} = 2\delta_{\max}/\pi$. During the Ir film deposition process using argon-ion discharge sputtering, the Ir atoms will deposit on the floss like snow precipitation. This makes the Ir film have the largest thickness on the top, and the least one on the side [as shown in figure 1(d)]. The measured properties are the effective properties of the overall films whose thickness ranges from 0 to the largest thickness. Afterwards, if not specially mentioned, the thickness will be the average thickness. In this work, the Ir films on milkweed fibers are coated using a sputtering machine (Quorum Q150T S). The thicknesses ($\delta_{\max}$) of the deposited Ir films are monitored using a quartz crystal microbalance. The accuracy of the thickness measurement is verified by an atomic force microscope.

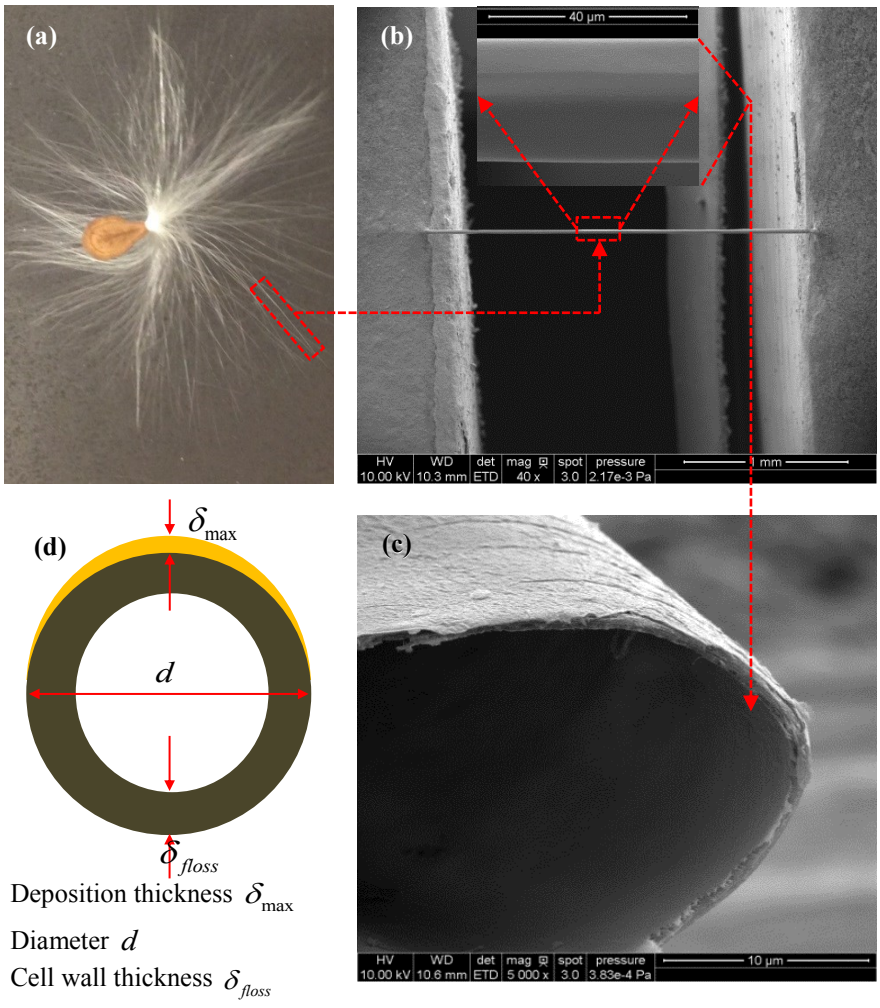


Figure 1. (a) A milkweed seed and floss. (b) SEM image of a single milkweed fiber suspended across two electrodes (the long sample). The inset shows the floss surface. (c) SEM image of the milkweed fiber cross section. (d) Profile of the milkweed fiber cross section coated with a layer of Ir, and the definition of maximum thickness $\delta_{max}$. The average thickness of the Ir film is $\delta_{ave} = 2\delta_{max}/\pi$.

It should be pointed out that the floss surface is not atomic-level smooth although the Ir sputtering machine can deposit very fine grains on the floss surface. Also the sputtered layer cannot reach atomic level uniformity. In our previous work (the supporting information of

reference [26]), we checked the surface roughness of 1 nm Ir film with AFM. The results showed that the roughness of the film is about ±0.4 nm. So the surface is not atomic smooth but the surface is not very rough. What is more, in this work we deposited a 15 nm Ir film first to guarantee that the film had steady electrical resistance and all the second, third and fourth films contributed to thermal and electrical transport. Therefore, the average thickness refereed in this work represents an average value: a value that is obtained by the deposition mass divided by the projected area in the deposition direction. The thicknesses in the deposition direction ($\delta_{\max}$) of the deposited Ir films are monitored using the quartz crystal microbalance whose accuracy was verified by an AFM. Still the film shows high-level thickness uniformity as shown in figure 2(b), which will be discussed later. From that figure, it is clear the Ir film (32 nm average thickness in TEM study) is continuous along the surface of the floss surface, and it shows nm-scale surface smoothness.

Here we choose milkweed floss as the substrate material due to several reasons. First, the milkweed floss is a unique natural cellulose fiber that has a low density due to the presence of a completely hollow center.[30-32] No other known natural cellulose fiber has such an overall low density.[30] Consequently it will have a very low overall thermal conductivity. This will provide a great advantage for studying the Ir film on it because the overall thermal diffusivity would have a great increase even when a very thin Ir film is deposited on it. Second, the fiber surface is smooth and its diameter is very uniform and well defined, as shown in the inset of figure 1(b). This ensures accurate control and measurement of the metallic film's geometry. Milkweed floss is a single-cell fiber,[30] so our experiment can provide fundamental information about the energy transport capacity along single plant cell wall as the byproduct. Furthermore, milkweed floss has been used or reported as textiles and filling material.[32-35] Plant cell fibers composed

of cellulose and lignin also could be an excellent platform for flexible electronics. Therefore, it is of great interest to investigate the heat conduction in Ir films grown on it, as well as its own thermal properties.

As shown in figure 1(c), the milkweed fiber is hollow. Under a scanning electron microscope (SEM), the average milkweed wall thickness is determined as 614 nm. In this work, four sets of experiments are conducted from room temperature down to 10 K. 10 K is the lowest temperature the sample could stay. When the temperature is lower than 43 K, the electrical resistance does not change with temperature linearly, and also has very weak temperature dependence. Therefore, the TET technique cannot be used to characterize the thermal diffusivity accurately. First, after the milkweed fiber is coated with the first Ir layer with an average thickness of 9.6 nm, the effective thermal diffusivity is measured from room temperature to 43 K. Then the temperature is allowed to rise slowly to room temperature. We have confirmed that the electrical resistance of the sample at room temperature remains unchanged after the sample experiences the extremely low temperature environment. This firmly concludes that the structure of the milkweed and Ir film on it is unchanged in our thermal characterization from room temperature to 10 K. After the first round of measurement is done, a second layer of Ir with an average thickness of 3.2 nm (whose $\delta_{max}$ is 5 nm) is coated. Subsequently, the measurement is repeated from room temperature to 10 K. Then again the temperature goes back to room temperature slowly. These measurement processes are repeated four times and the third and fourth Ir layers are the same as the second one. During these processes, the structure of milkweed and Ir films are not affected by the low temperature. This is critical to ensure the properties of the four ultra-thin films are the same.

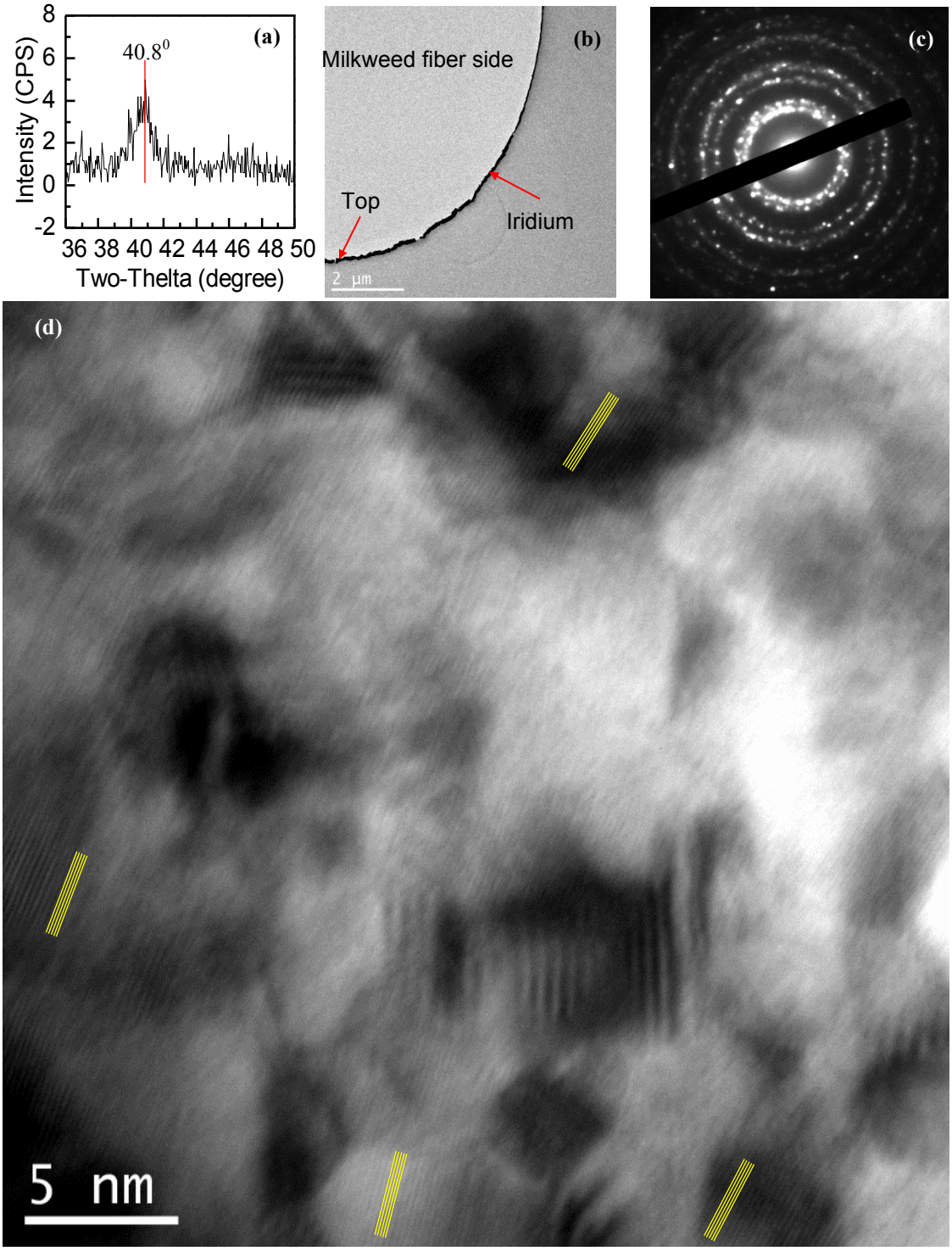


Figure 2. (a) XRD pattern of 10 layers of 3.2 nm-thick Ir films on milkweed fibers. The peak appears at 40.8°, which indicates that the Ir film is composed of crystals. The crystalline size is estimated at about 8 nm. (b) Low-magnified TEM image of 10 layers of 3.2 nm-thick Ir films coated on milkweed fibers. (c) The diffraction pattern of 10 layers

of 3.2 nm-thick Ir films. The bright spots in the diffraction pattern show the existence of nanocrystals clearly. (d) High-resolution TEM picture of the Ir film. The yellow parallel lines show the lattice orientation.

To characterize the structure of milkweed fibers and the Ir films on it, X-ray diffraction (XRD) is used. The XRD system (Siemens D 500 diffractometer) is equipped with a copper tube that was operated at 40 kV and 30 mA. Because one milkweed fiber is too small compared with the XRD spot size, we use a bunch of milkweed fibers and align them parallel to each other. These fibers are suspended and scanned by XRD. They are confirmed amorphous. To obtain the structure information of the Ir film, a layer of 3.2 nm-thick Ir film ($\delta_{ave} = 3.2\,\text{nm}$ and $\delta_{\max} = 5\,\text{nm}$) is not enough to generate a sufficient XRD signal. So these fibers are coated with 10 layers of 3.2 nm-thick Ir films and scanned for XRD again. The result is shown in figure 2(a). The peak appears at 40.8°, which indicates that the film is composed of crystals. The crystalline size is estimated to be about 8 nm.

Additionally, after XRD characterization, the same sample is studied by TEM (a JEOL 1200EX TEM with a 1.4 Å resolution). For the TEM sample preparation, a liquid resin is used with plasticizers and then mixed together with milkweed fibers. They are put into a vacuum chamber to drive air out of the liquid and the liquid flows into the hollow part of the fibers. This liquid mixture is poured in a mold and allowed to slowly polymerize at room temperature. After the solidification, this resin with fibers is sliced into thin pieces as the samples for TEM study. The low-magnified TEM images of 10 layers of 3.2 nm-thick Ir films coated on milkweed fiber is shown in figure 2(b). We can see the maximum film thickness appears at the top and the thickness decreases gradually. Figure 2(c) shows the diffraction pattern of 10 layers of 3.2 nm-thick Ir films. The bright spots in the diffraction pattern show the existence of nanocrystals clearly. The high-resolution TEM image is shown in figure 2(d). The yellow parallel lines show

the lattice orientation. The different orientations of the lattice confirm the nanocrystalline structure of the Ir films on milkweed fiber.

## 2.2. Differential Technology for Electrical and Thermal Characterization

A robust and advanced differential technology,[26, 29] has been developed in our lab to characterize the thermal properties of ultra-thin metallic films. The measured film thickness can reach sub-5 nm while other technologies cannot achieve this level. In this work, a milkweed fiber is suspended across two electrodes as the supporting material for the ultra-thin metallic films as shown in figure 3(b).

For thermal characterization of a one-dimensional material by using the TET technique, the material has to be electrically conductive. Therefore, the milkweed fiber is first coated with a Ir film of thickness $\delta_1$ (the first layer) and the effective thermal diffusivity of the milkweed fiber-metallic film system in the axial direction is measured as $\alpha_{eff,0}$. Also the electrical resistance of the film can be readily measured as $R_0$. Then the same sample is coated with a second Ir layer of thickness $\delta_2$, and the whole sample's thermal diffusivity and resistance are measured again as $\alpha_{eff,1}$ and $R_1$. The thermal diffusivity increment induced by the second Ir layer is $\Delta\alpha_{eff} = \alpha_{eff,1} - \alpha_{eff,0}$. This thermal diffusivity differential is directly related to the Lorenz number of the second Ir layer of thickness $\delta_2$, and other parameters of the sample, like the milkweed fiber's geometry and thermal properties. Theoretically, to measure the electrical and thermal conductivities, and the Lorenz number of the second Ir layer of thickness $\delta_2$, only one second layer ($\delta_2$ thickness) needs to be coated. To improve the measurement accuracy and significantly suppress experimental uncertainty, we repeatedly deposit Ir layers of thickness $\delta_2$ and measure the corresponding thermal diffusivity $\alpha_{eff,n}$ and the electrical conductance $G_n$ ( $R_n^{-1}$ ).

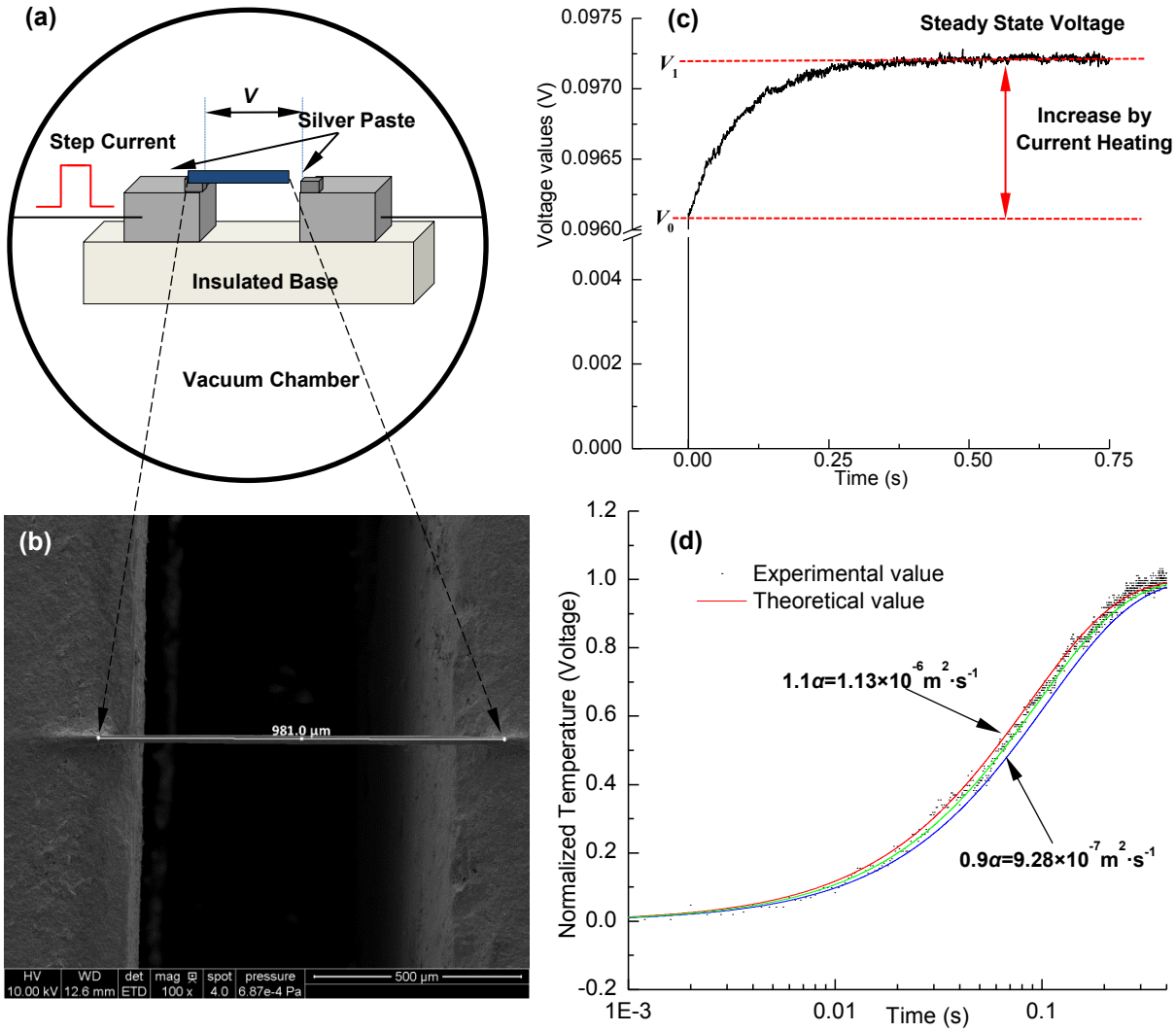


Figure 3. (a) Schematic of the experimental principle of the TET technique to characterize the thermal diffusivity of the sample. (b) SEM image of a coated milkweed fiber connected across two electrodes (the short sample). (c) A typical *V-t* profile recorded by the oscilloscope for the sample shown in figure (b) induced by the step DC current. The result is for the sample coated with the first Ir layer ($\delta_{1,max}$=15 nm). (d) TET fitting results for the sample at room temperature. The figure consists of the normalized experimental temperature rise, theoretical fitting results, and other two fitting curves with ±10% variation of $\alpha_{eff}$ to demonstrate the variation of the experimental data around the best theoretical fitting.

After that, the thermal diffusivity and electrical conductance increments can be obtained respectively ( $\Delta\alpha_{eff}$ and $\Delta G$ ). The thermal conductivity ( $\kappa$ ) of a single $\delta_2$-thick Ir layer is determined based on the increment of thermal diffusivity ($\Delta\alpha_{eff}$). Details can be found in reference[36]. Then the Lorenz number ($L_{\mathrm{Lorenz,B}}$) of a single Ir layer with a thickness of $\delta_2$ can be determined precisely. Here, both $\delta_1$ and $\delta_2$ refer to the maximum thickness of the Ir films. The first Ir layer ($\delta_1$ thickness) is used to make the sample electrically conductive. So the thickness of this layer can be the same or different from $\delta_2$. In this work, $\delta_1$ is chosen to be 15 nm, which is thick enough to obtain a stable electrical resistance of the sample. $\delta_2$ is 5 nm and three layers of Ir films with thickness of $\delta_2$ are deposited layer by layer on the first layer. It is physically reasonable that each deposited Ir layer ($\delta_2$ thickness) has the same thermal properties because they have the same thickness and are deposited under the exactly same conditions. This assumption is fully checked and verified by the experimental results and discussed later. Details of the theory and experimental process for this differential technology are given in below.

The measured thermal diffusivity ($\alpha_{eff}$) is an effective value combining both effects of the milkweed fiber and Ir coatings.

$$\alpha_{eff} = \frac{A_m\kappa_m + A_1\kappa_1 + nA_2\kappa_2}{A_e(\rho c_p)_e}, \tag{1}$$

where $n$ is the number of $\delta_2$ thick layers. $A_e$, $A_m$, $A_1$, and $A_2$ are the cross-sectional area of the coated fiber, bare fiber (including the hollow region), the first Ir layer, and an individual $\delta_2$ thickness Ir layer. The thin Ir layer has negligible contribution to the overall cross-sectional area of the sample, so we have $A_e$=$A_m$. Moreover, the contribution of ultra-thin Ir films to volumetric specific heat is negligible (~1%), so we take the volumetric specific heat to be unchanged ( $(\rho c_p)_e$=$(\rho c_p)_m$ ). $\alpha_{eff}$ increases with the number of film layers and the slope is $A_2\kappa_2/A_e(\rho c_p)_e$ .

$A_2/A_e(\rho c_p)_e$ is known already so the thermal conductivity ($\kappa_2$) of the 3.2 nm-thick Ir film can be determined.

### 2.2.1 TET technique for thermal characterization of Ir-coated floss

The TET technique [37, 38] developed in our laboratory is used to measure the effective thermal diffusivity ($\alpha_{eff}$) of the Ir-covered milkweed fiber. A schematic of the TET technology is presented in figure 3(a). The to-be-measured sample is suspended across two aluminum electrodes, and placed in the vacuum chamber of a cryogenic system (CCS-450, JANIS). To eliminate heat convection in the measurement, a liquid nitrogen cold-trapped mechanical vacuum pump is used to reach a vacuum level of 0.4 mTorr. During thermal characterization, a step DC current is fed through the sample to generate electric heat that induces a temperature rise of the sample. The temperature rise of the sample will induce an electrical resistance change, which leads to an overall voltage change. Therefore, the voltage change of the sample can be used to monitor its temperature evolution, and determine the thermal diffusivity of the sample. Details of the experimental process and data reduction are given in below.

During TET thermal characterization, the average temperature along the sample can be expressed as:

$$\overline{T} = T_0 + \frac{q_0 L^2}{12}\frac{48}{\pi^4}\sum_{m=1}^{\infty}\frac{1-(-1)^m}{m^2}\frac{1-\exp\left[-\left(m^2-f\right)\pi^2(\alpha t/L^2)\right]}{(m^2-f)}. \quad (2)$$

As time goes to infinity, the temperature distribution along the sample will reach a steady state. The average temperature of the sample in the final steady state is:

$$T(t\to\infty) = T_0 + \frac{q_0 L^2}{12k}. \quad (3)$$

More details for the above equation's derivation are provided in references [37, 39]. With an effective thermal diffusivity $\alpha_{eff}=\alpha\cdot(1-f)$, here $f$ is defined as $-8\varepsilon_r\sigma T_0^3 L^2/d\pi^2 k$ (the radiation effect), the normalized average temperature rise $T^*$ is:

$$T^* \cong \frac{48}{\pi^4}\sum_{m=1}^{\infty}\frac{1-(-1)^m}{m^2}\frac{1-\exp[-m^2\pi^2\alpha_{eff}t/L^2]}{m^2}. \quad (4)$$

The measured voltage change is inherently proportional to the temperature change of the sample. The normalized temperature rise $T^*$ is calculated from experiment as $T^*=(V_{sample}-V_0)/(V_1-V_0)$, where $V_0$ and $V_1$ are the initial and final voltages across the sample. In our work, after $T^*$ is obtained, different trial values of $\alpha_{eff}$ are used to calculate the theoretical $T^*$ using equation (4) and fit with the experimental result. The value giving the best fit of $T^*$ is taken as the effective thermal diffusivity of the sample.

Here we take the sample at room temperature as an example to demonstrate how the effective thermal diffusivity is characterized. The length and diameter of this sample is 981 μm and 20.53 μm respectively. The sample is coated with the first Ir layer ($\delta_{1,ave}$=9.6 nm). The electrical resistances before and after applying a step current are 615.99 Ω and 623.15 Ω. The electrical current used in the experiment is 156 μA. This gives a voltage change at about 1% due to self-joule heating.

Figure 3(c) shows the transient voltage change of raw experimental data. The normalized temperature rise and the fitting result are shown in figure 3(d). The effective thermal diffusivity is determined as $1.03\times10^{-6}$ $m^2\cdot s^{-1}$, which includes the effect of radiation and parasitic conduction. We vary the trial values of $\alpha$ to determine the fitting uncertainty as shown in figure 3(d). When the trial value is changed by 10%, the theoretical results deviate from the experimental results

evidently. It is evident that the experimental data falls within a range of ±10% of the theoretical fitting.

## 2.3. Electrical Transport in Ir Film

### 2.3.1. Determination of electrical resistivity of individual Ir film

Electrical resistance is readily obtained when the electrical current and voltage through the sample are measured during TET characterization. The inset of figure 4 depicts the temperature dependent electrical resistance of the floss sample coated with different Ir films. As we can see from the inset of figure 4, when the temperature is not very low (> 35 K), the electrical resistances rise with increasing temperature linearly. When temperature is lower than 20 K, the electrical resistance behaves temperature-independent: a residual resistance shows up. In this figure, after more 3.2 nm-thick Ir films are coated on the sample, its electrical resistance becomes smaller. Also the rate that the resistance changes against temperature is different for the samples. Sole study of the electrical resistance and its change against temperature reveals little understanding of the electron transport. Therefore we calculate the electrical conductance and uncover more insight into the electron transport and scattering.

According to $G_n = R_n^{-1}$, here $R$ is the measured electrical resistance of the sample, the effective electrical conductance of the films are calculated and depicted in figure 4. It is related to the film number $n$ as

$$G_n = \frac{d\delta_{1,\max}}{L\rho_1} + \frac{nd\delta_{2,\max}}{L\rho_2}, \tag{5}$$

where $\rho_1$ is the electrical resistivity of the base layer ($\delta_{1,ave} = 9.6\,\text{nm}$ and $\delta_{1,max} = 15\,\text{nm}$); $\rho_2$ is the electrical resistivity of a single Ir layer with $\delta_{2,ave} = 3.2\,\text{nm}$ ($\delta_{2,max} = 5\,\text{nm}$); $n$ is the number of the

$\delta_{2,ave}=3.2$ nm Ir layer and $d$ is the outside diameter of the milkweed fiber. Figure 4 shows that the $G_n$ increase induced by each average 3.2 nm-thick Ir layer is constant in our experiment. This firmly confirms the point that the 3.2 nm Ir layers studied in this work have the same structure and properties. Based on this electrical conductance increase, the electrical resistivity of an individual average 3.2 nm-thick Ir layer can be readily determined.

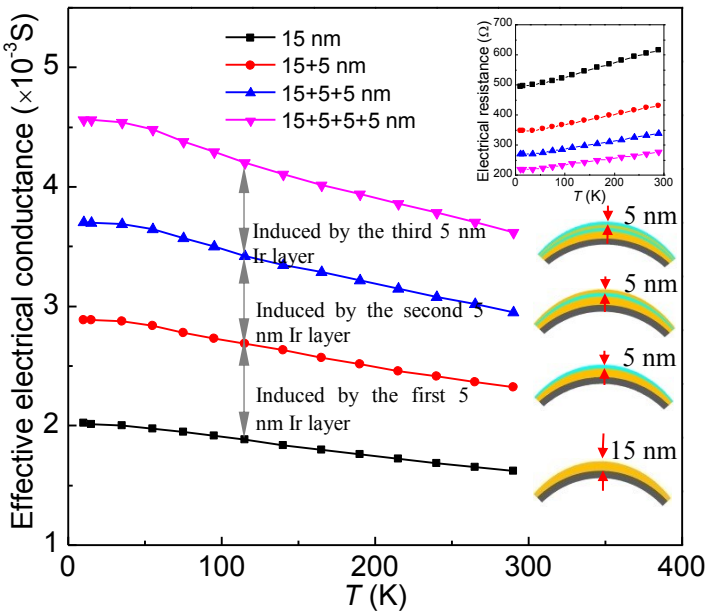


Figure 4. The effective electrical conductance of the ultra-thin Ir films coated on the milkweed floss. The inset depicts the temperature dependent effective electrical resistance of the ultra-thin Ir films. Here, "5 nm and 15 nm" refers to the maximum thickness of the Ir film.

It is seen from equation (5) that the slope of the effective electrical conductance changing against $n$ is only related to the electrical resistivity of a single average 3.2 nm-thick Ir film. By fitting the change of $G_n$ against $n$, we can obtain the slope of the fitting line and then the electrical resistivity of a single average 3.2 nm-thick Ir film is determined as $\rho_2=d\delta_{2,\max}/(L\cdot slope)$

. The electrical resistivity of a single average 3.2 nm-thick Ir film from room temperature down to 10 K is determined. The result is shown in figure 5 in comparison with the bulk's value. The inset in the bottom right corner of figure 5 shows the linear fitting on determining the electrical resistivity of a single average 3.2 nm-thick Ir film at room temperature. It can be seen that the fitting is excellent and each single average 3.2 nm-thick Ir film indeed has the same electrical resistivity. This echoes the point we just claimed above that each average 3.2 nm-thick Ir film has the same structure and property.

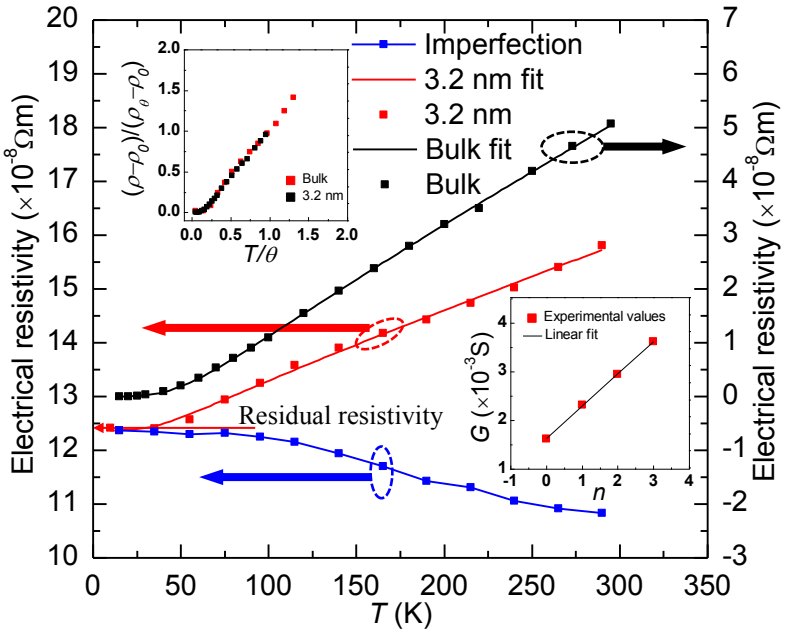


Figure 5. Temperature dependence of electrical resistivity of a single 3.2 nm-thick Ir film, its imperfection part and bulk Ir. [1]The inset in the upper left corner shows the normalized electrical resistivity against normalized temperature. The inset in the bottom right corner depicts one of the linear fittings used to determine the electrical resistivity of a single 3.2 nm-thick Ir film.

Also shown in figure 5 is the electrical resistivity of bulk Ir for comparison. The electrical resistivity of a single average 3.2 nm-thick Ir film is much larger than that of bulk Ir. This is

mainly due to the size and structural effect. Specifically, the grain boundary area per unit volume increases significantly when the film thickness goes down to sub-5 nm. The grain boundary scattering impedes the electron transport in the film, which considerably contributes to the increase in electrical resistivity. Furthermore, the large surface-to-volume ratio of the film intensifies electron surface scattering, which also increases the electrical resistivity. These scattering sources result in the large electrical resistivity of a single 3.2 nm-thick Ir film. These general physics will be elucidated below.

### 2.3.2. Behavior of electron transport under reduced temperatures

As we can see from figure 5, for an individual average 3.2 nm-thick Ir film, the slope of electrical resistivity against temperature is smaller than that of the bulk Ir. Here, we designate this slope as the temperature coefficient of electrical resistivity (TCER). A reduced TCER also has been observed for nanocrystalline nickel with a thickness of 30 nm, but little attention has been paid to it.[40] In reference [41], for $Sn_{0.84}Cu_{0.16}$ alloy the TCER of the amorphous state is much smaller than that of the polycrystalline state. In reference [42], the TCER of 180 nm copper film is smaller than that of 645 nm. The reduced TCER is due to the reduced electron-phonon coupling parameter and the reduced Debye temperature which will be discussed in detail later.

The electrical resistivity of the average 3.2 nm-thick Ir film can be expressed by the Matthiessen's rule and the Bloch-Grüneisen theory [43] as

$$\rho=\rho_0+\rho_{el-ph}, \tag{6}$$

$$\rho_{el-ph}=\alpha_{el-ph}\left(\frac{T}{\theta}\right)^n\int_0^{\theta/T}\frac{x^n}{\left(e^x-1\right)\left(1-e^{-x}\right)}dx, \tag{7}$$

where $\rho_0$ is the residual resistivity which results from grain boundary, impurities, surface scatterings and so on. It is essentially temperature independent. $\rho_{el-ph}$ is the electrical resistivity induced by phonon scattering, which is temperature dependent. $\alpha_{el-ph}$ is the electron-phonon coupling parameter. $\Theta$ is the Debye temperature and $n$ generally takes the value of 5 for nonmagnetic metals with a reasonable mean free path.[20] The scattering rate for phonon-electron scattering is proportional to the number of occupied phonon states. At high temperatures this number increases linearly with increasing temperature. That is why the electrical resistivity increases linearly with increasing temperature at high temperatures. The number of phonons increases proportionally to $T^3$ at low temperatures. An angle dependence weighting factor for the scattering processes needs to be considered, which is proportional to $T^2$. Therefore, at low temperatures the electrical resistivity is proportional to $T^5$.[44], The phonons are frozen out when the temperature goes extremely low and $\rho_{el\text{-}ph}$ becomes negligible near absolute zero. So the residual resistivity can be readily identified by evaluating the resistivity at very low (close to 0 K) temperatures. According to figure 5, the residual resistivity ($1.24\times10^{-7}$ Ωm) of the 3.2 nm-thick Ir film is much larger than that of the bulk material (almost zero). This is due to the increased electron scattering by the increased grain boundary, surface and impurities when the film is ultra-thin.

The electrical resistivity of a 3.2 nm-thick Ir film measured in this work and that of bulk Ir in reference [1] are both fitted with the Bloch-Grüneisen formula. The fitting results are summarized in table 1. Also figure 5 confirms the experimental data can be very nicely fitted using the Bloch-Grüneisen formula. The residual resistivity of the bulk Ir is approximately zero, which indicates that the effect of grain boundary, surface and impurities are negligible and the sample is of high purity. On the other hand, the residual resistivity of the 3.2 nm-thick Ir film is

about $1.24\times10^{-7}$ Ω·m, dominating the overall resistivity. $\alpha_{el-ph}$ ($2.24\times10^{-7}$ Ω·m) of bulk Ir is approximately twice as large as that of the 3.2 nm-thick Ir film ($1.06\times10^{-7}$ Ω·m). This is due to phonon softening which leads to the reduced phonon frequency, phonon number and subsequently changed electron-phonon coupling.

**Table 1.** Bloch-Grüneisen Formula Fitting parameters for the 3.2 nm-thick Ir film and bulk Ir.

| $\delta$ (nm) | $\rho_0$ (Ω·m) | $\alpha_{el-ph}$ (Ω·m) | $\theta$ (K) | $\rho_\theta$ (Ω·m) | $\alpha_R$ |
|---|---|---|---|---|---|
| Bulk | 1E-11 | 2.24E-7 | 307.9 | 5.32E-08 | 4.207 |
| 3.2 | 1.24E-07 | 1.06E-7 | 221.4 | 1.48E-07 | 4.355 |

The Debye temperatures are obtained through fitting the variation of electrical resistivity versus temperature. Specifically, the Debye temperature of bulk Ir is determined as 307.9 K, which is close to the value (290 K) of bulk Ir in [1]. But this value is still much smaller than the value (420 K) obtained by fitting specific heat.[45] The Debye temperature of the 3.2 nm-thick Ir film in this work is 221.4 K, which is much smaller than its bulk counterpart. The reduced Debye temperature is due to phonon softening which results from several factors. Specifically, the atoms at the surface have a lower coordination number than the bulk material. The missing bonds result in the change of vibration amplitude and subsequently the vibration frequency and Debye temperature. When the film is ultra-thin, the large surface-to-volume ratio leads to significant phonon softening. Moreover, internal surfaces, such as grain boundary and point defects, also can soften phonons and contribute to the decrease of the Debye temperature. Similar phenomenon is also observed in gold, platinum, copper, silver nanofilms or nanowires, and cobalt/nickel superlattices.[18-20, 46-48]

The phonons that contribute to the electron-phonon interaction are the acoustic phonons based on the Bloch-Grüneisen theory.[20] Then for the temperature dependent part of electrical resistivity, we can get the equation below:

$$\frac{\rho_{el-ph}}{\rho_{el-ph,\theta}} = \frac{\rho - \rho_0}{\rho_\theta - \rho_0} = \alpha_R \left(\frac{T}{\theta}\right)^n \int_0^{\theta/T} \frac{x^n}{\left(e^x - 1\right)\left(1 - e^{-x}\right)} dx \,, \tag{8}$$

where $\rho_{el-ph,\theta}$ is the temperature dependent electrical resistivity at the corresponding Debye temperature.

The electrical resistivity of the bulk Ir and the 3.2 nm-thick Ir film at Debye temperatures are shown in table 1. Then the values of $\alpha_R$ for the bulk material and the average 3.2 nm-thick Ir film are determined and shown in table 1. They are almost the same and equal the value (4.225) predicted by the simple acoustic phonon-electron coupling theory.[49] The right side of equation (8) is only related to the Debye temperature $\theta$. Therefore, the measured electrical resistivity can be scaled using equation (8). The scaled results are shown in the upper-left inset in figure 5. The scaled electrical resistivity of the 3.2 nm-thick Ir film and bulk Ir agrees very well with each other. This proves that it is applicable to use the Bloch-Grüneisen formula to interpret the results for the 3.2 nm Ir film. It is conclusive that phonon-electron scattering makes the dominant contribution to the temperature-dependent electrical resistivity in the temperature range in this work.

In our past works about ultra-thin metallic films, [26, 29] the electrical and thermal conductivities are not sensitive to the film thickness. So the surface scatterings can be considered as specular. According to the Mayadas-Shatzkes (MS) Model, [50, 51] the electron reflection coefficient can be determined. For our film, its value ranges from 0.86 at room temperature to 0.88 at 82 K. In this temperature range, it is almost a constant. When temperature goes below,

the MS model is not applicable because the film thickness is too small compared with the bulk electron mean free path at the corresponding temperatures.

## 2.4. Thermal Transport in the Ir Film

### 2.4.1 Effective thermal diffusivity increments induced by the Ir films

The effective thermal diffusivity of the sample is characterized with the TET technique from room temperature down to 10 K. When the temperature is lower than 43 K, the electrical resistance does not change with temperature linearly, and also has very weak temperature dependence. Therefore, the TET technique cannot be used to characterize the thermal diffusivity accurately. The measurement results are shown in figure 6. The effective thermal diffusivity increases with decreasing temperature. The lower the temperature is, the faster the thermal diffusivity rises.

As we can see from figure 6, the effective thermal diffusivity increases by the same amount when each average 3.2 nm-thick Ir film is added on the sample. The solid curves represent the trends of the effective thermal diffusivity change with temperature. Every time an average 3.2 nm-thick Ir film is added, the effective thermal diffusivity increment is denoted as $\Delta\alpha_{eff,1}$. The inset in figure 6 shows the change of thermal diffusivity at room temperature against the number of average 3.2 nm-thick Ir films. An excellent linear trend is observed. This strongly proves that each layer has the same thermophysical property. The effective thermal diffusivity increment induced by each Ir layer at low temperatures bears a little more noise/uncertainty. Therefore, we use the effective thermal diffusivity increment ($\Delta\alpha_{eff}$) between the fourth layer and the first layer case to determine the thermal transport properties of the Ir film. This data treatment maximizes the thermal diffusivity difference and efficiently suppresses measurement uncertainty. As we can see from figure 6, $\Delta\alpha_{eff}$ shows weak temperature dependence and changes

linearly with temperature. Also the uncertainty in the data becomes small, which is more tolerable. A linear fitting is used to smooth the effective thermal diffusivity difference $\Delta\alpha_{eff}$ and the result will be used for thermal conductivity determination of the Ir film.

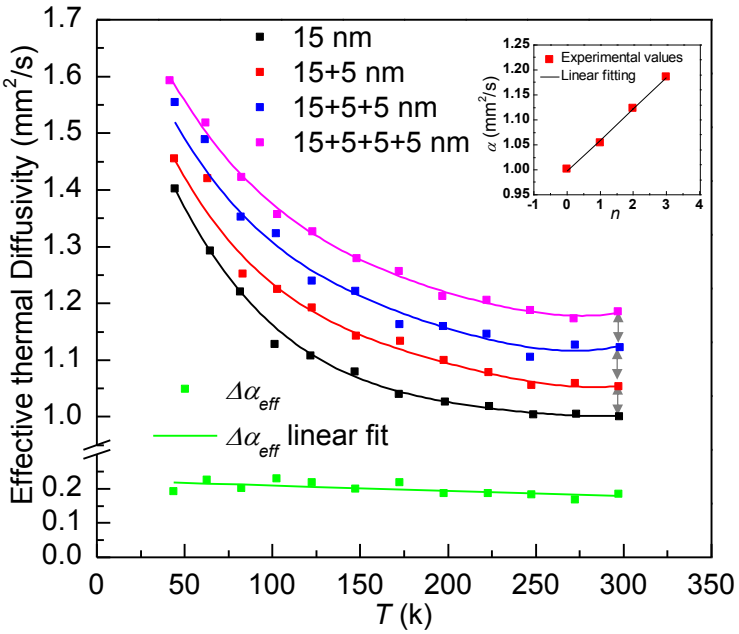


Figure 6. Measured effective thermal diffusivity of the milkweed floss coated with different layers of Ir films. "$\Delta\alpha_{eff}$" is the effective thermal diffusivity difference between the 19.2 nm film ("15+5+5+5 nm" case whose $\delta_{ave}$=19.2 nm) and 9.6 nm film ("15 nm" case whose $\delta_{ave}$=9.6). "$\Delta\alpha_{eff}$ linear fit" represents linear fitting of "$\Delta\alpha_{eff}$" variation against temperature. "$\Delta\alpha_{eff,1}$" is the effective thermal diffusivity increment induced by each 3.2 nm-thick Ir layer. The solid curves are to show the trends of effective thermal diffusivity changing with temperature. The inset shows the thermal diffusivity changes against the number of film layers linearly to demonstrate that each 3.2 nm-thick Ir film indeed has the same thermal conductivity, and follows the theory expressed by equation (1).

### 2.4.2 Thermal conduction

Based on $\Delta\alpha_{eff}$ induced by the three 3.2 nm-thick Ir films, we could find the thermal conductivity $\kappa$ of an individual Ir film as $\kappa=\left(\rho c_p\right)_m \cdot (A_m/A_2)\cdot\left(\Delta\alpha_{eff}/3\right)$. In this equation, $A_m/A_2$ is the cross-sectional area ratio of the sample to the 3.2 nm-thick Ir film. The effective thermal diffusivity increment induced by each 3.2 nm-thick Ir film is $\Delta\alpha_{eff}/3$ because each 3.2 nm-thick Ir film has the same thermal conductivity, which is verified by experimental results shown in figure 6. $\left(\rho c_p\right)_m$ is the effective volumetric specific heat of the sample. To determine the thermal conductivity of an individual Ir layer, the effective volumetric specific heat $\left(\rho c_p\right)_m$ of the sample is needed. So we must determine this property in advance. Details on how this property is determined are given in below.

During TET characterization, the average temperature rise is $\Delta T = q_0 L^2/12k_{eff}$ according to equation (3), here $q_0=4I^2R/\pi d^2 L$ is the heat generation per unit volume. The temperature rise during our TET characterization can be obtained from the electrical resistance change ( $\Delta R$ ) as $\Delta T = \Delta R/(\eta R_0)$. $\eta$ is the temperature coefficient of resistance. Then we can obtain the effective thermal conductivity $k_{eff} = q_0 L^2/12\Delta T$. As the effective thermal diffusivity has been determined for each round of experiment (figure 6), the volumetric specific heat $\left(\rho c_p\right)_m = \kappa_{eff}/\alpha_{eff}$ can be obtained. The volumetric specific heat of the milkweed fiber is determined four times because the contribution of the ultrathin metallic films to the total volumetric specific heat is negligible (the maximum average contribution of Ir is ~1%).

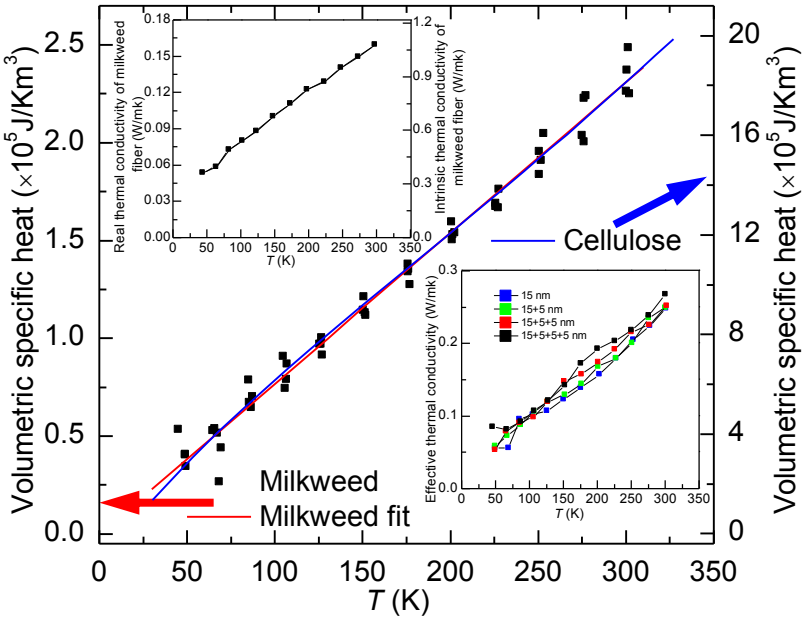


Figure 7. Temperature dependent volumetric specific heat of milkweed and microcrystalline cellulose. [2] The inset in the upper left corner shows the effective and intrinsic thermal conductivity of the milkweed fiber. The inset in the bottom right corner shows the effective thermal conductivity of the Ir-coated milkweed fiber.

The specific heat shown in figure 7 shows a good linear relation with temperature, so a linear fitting is used to smooth the data for later use. The volumetric specific heat of milkweed fiber decreases with decreasing temperature. This is because the short wave phonons are frozen out and only the long wave phonons are excited to contribute to the specific heat. In figure 7, the volumetric specific heat of milkweed fiber is compared with that of the microcrystalline cellulose in literature.[2] It can be seen that the two lines overlap using different vertical coordinates, which means the trends of volumetric specific heat against temperature are the same for the milkweed fiber and the microcrystalline cellulose. Using the volumetric specific heat of microcrystalline cellulose as the reference, then we can obtain the volumetric ratio of the cell wall as 12.85%. Subsequently, the cell wall thickness is determined as 660 nm, which is only 7% larger than our SEM measurement result (614 nm). The measured thickness (614 nm) is smaller

than the expected thickness (660 nm) based on the assumption that the thermal property of milkweed cell wall is similar to that of the microcrystalline cellulose. This means the real volumetric specific heat of the milkweed cell wall is larger than that of the microcrystalline cellulose. This can be explained by several reasons. First, the contribution of metallic film gives some contribution to this difference. Furthermore, the specific heat of the amorphous state is usually larger than that of the crystalline state. Finally, the cell wall contains other materials apart from cellulose, like lignin and hemicellulose. The specific heats of these materials also affect the overall specific heat.

The inset in the bottom right corner of figure 7 shows the effective thermal conductivity for the four cases. The real thermal conductivity of the milkweed fiber (including the effect of the hollow center) can be obtained by subtracting the effects of the Ir films and radiation. The intrinsic thermal conductivity of the milkweed fiber can be determined after the volumetric ratio of the milkweed cell wall is known. Details are described below and the results are shown in the inset in the upper left corner of figure 7.

To obtain the real and intrinsic thermal conductivity of the milkweed floss, we need to subtract the effect of radiation. Experiment on a long sample is conducted to determine the surface emissivity $\varepsilon_r$ based on $k_{real} = \alpha_{eff,n}\rho c_p - 16\varepsilon_r \sigma_{SB} T_0^3 L_n^2 / (d_n \pi^2) - 4L_{Lorenz} T_n L_n / (R_n \pi d_n^2)$ . Subscript *n* takes 1, 2, referring to the long sample and the sample used above, respectively. $\sigma_{SB}$ is the Stefan-Boltzmann constant. We use the volumetric specific heat of the sample used above [$2.33\times10^5$ J/(K·m$^3$)] and the Lorenz number [$2.29\times10^{-8}$ W·Ω·K$^{-2}$] to calculate the emissivity. The length and diameter of the long sample are 2366 μm and 23.99 μm respectively. The effective thermal diffusivity of the long sample and the sample used above are $1.71\times10^{-6}$ m$^2$·s$^{-1}$ and $1.00\times10^{-6}$ m$^2$·s$^{-1}$ respectively. Only the real thermal conductivity of the milkweed fiber $k_{real}$ and

surface emissivity $\varepsilon_r$ are unknown in the two equations above and the surface emissivity is determined as 0.40.

The real thermal conductivity of the milkweed fiber can be determined after subtracting the effect of radiation and parasitic conduction of the metallic film as $\kappa_{real} = \kappa_{eff} - 16\varepsilon_r \sigma_{SB} T_0^3 L^2 / (d\pi^2) - 4L_{Lorenz} TL / (R\pi d^2)$. The real thermal conductivity of the milkweed fiber is obtained and depicted in the inset in the upper left corner of figure 7. Because we know the thickness of the cell wall through SEM measurement, the volumetric ratio is obtained as 14.78%. The intrinsic thermal conductivity of the milkweed cell wall is also determined by dividing $k_{real}$ by 14.78% and shown in the inset in the upper left corner of figure 7 using the right coordinate axis.

The thermal conductivity of milkweed fiber decreases with decreasing temperature. The thermal conductivity shows a similar trend with the volumetric specific heat, namely changing linearly with temperature. Theoretically, we can determine the thermal conductivity of an individual Ir film by examining the thermal conductivity increment by the addition of each Ir film. However, as shown in the inset in the bottom right corner of figure 7, the thermal conductivity data barely reveals good enough data to calculate the increment. The effective thermal conductivity data carries much more uncertainties than thermal diffusivity. This is because the thermal conductivity evaluation relies on more data, like electrical resistance temperature coefficient, resistance rise in experiment, and electrical heating level. So we do not use the directly measured effective thermal conductivity to evaluate the thermal transport in the Ir film.

Based on the volumetric specific heat (figure 7) and $\Delta\alpha_{eff}$ (figure 6), the thermal conductivity ($\kappa$) of an individual 3.2 nm-thick Ir film is calculated and shown in the left inset of

figure 8. The orders of magnitude reduction of the film's thermal conductivity in comparison with that of the bulk Ir is also obtained and shown in the right inset of figure 8. It can be seen that the thermal conductivity of the 3.2 nm-thick Ir film is significantly reduced from the bulk value. When temperature goes below 50 K, the thermal conductivity reduction reaches an extremely high level: close to two orders of magnitude. This is due to strong grain boundary scattering, which limits the electron mean free path significantly. For the bulk Ir, the short wave phonons are frozen out. Only long wave phonons contribute to the phonon-electron scatterings at low temperature. The decrease of scattering sources results in the increase of electron mean free path and subsequently thermal conductivity.

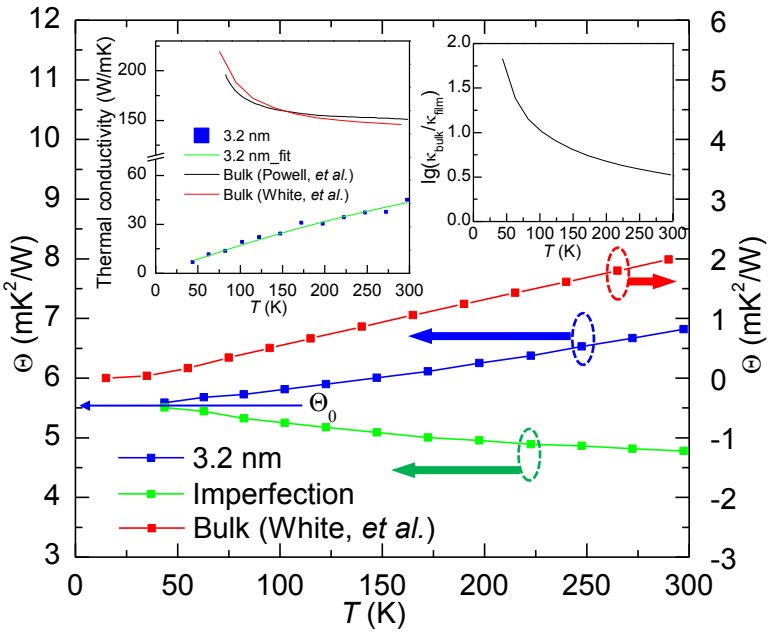


Figure 8. Temperature dependence of unified thermal resistivity of the 3.2 nm-thick Ir film and the bulk Ir (for comparison). [1]"3.2 nm" is the data calculated from the linearly fitted $\Delta\alpha_{eff}$ shown in figure 6. "Imperfection" represents $\Theta_{imper}$ induced by the imperfect structure in the film. The left inset shows the thermal conductivity variation against temperature and the right inset shows the orders of magnitude reduction of film's thermal

conductivity from that of bulk Ir (data from White, *et al.*). [1, 3] In the left inset, the "3.2 nm" depicts the thermal conductivity obtained directly from $\Delta\alpha_{eff}$ while the "3.2 nm_fit" shows the thermal conductivity obtained from the linear fitting values of $\Delta\alpha_{eff}$ (shown in figure 6).

For nanostructured metallic material, the phonon contribution to the overall thermal conductivity is larger than the bulk counterpart. At low temperatures, the phonon contribution to the thermal conductivity is significant but the electron contribution still dominates.[10] Here we take 43 K as an example to estimate the upper limit of the phonon thermal conductivity. The phonon heat capacity of Ir can be calculated by using the Debye Model [ $C_{ph,mole} = (12\pi^4 N_A k_B T^3)/(5T_D^3)$ ]. Here, $N_A$ is the Avogadro constant and $k_B$ is the Boltzmann constant. $T_D$ is the Debye temperature of Ir at low temperatures (420 K).[45] The molar mass of Ir is 192 g/mol and the density is $22.5\times10^3$ kg/m$^3$. We cannot find the phonon velocity of Ir so we use the sound velocity (4800 m/s) of Ir to estimate the thermal conductivity.[52] The phonon mean free path would be limited by the film thickness (3.2 nm). So the thermal conductivity ($\kappa = C_{ph,v} vl/3$) is determined as 1.25 W/m·K. Other scatterings like phonon-electron scattering, point defect-phonon scattering and phonon-phonon scattering would also limit the phonon mean free path. Its value should be smaller than 3.2 nm. So the thermal conductivity should be smaller than 1.25 W/m·K at 43 K. The measured thermal conductivity is 7.81 W/mK. Therefore, we can see from the comparison that phonon contribution to the overall thermal conductivity at low temperatures is significant but the electron contribution still dominates in the temperature range of this work.

The film's thermal conductivity decreases with decreasing temperature. This trend is completely opposite to that of the bulk Ir. This kind of phenomenon also has been observed in

gold and platinum nanofilms,[10, 53, 54] nickel nanowire[22] and alloys[55]. The reduced thermal conductivity was attributed to the increased scatterings of heat carriers from structural imperfection and the contribution of phonon thermal conductivity.[10, 22] Here we will provide an explanation of the abnormal temperature dependent thermal conductivity of these metallic nanostructures.

The thermal conductivity of electrons can be expressed as $\kappa=C_V v_F^2 \tau/3$. Here $C_v$ is the volumetric electron heat capacity; $v_F$ is the Fermi velocity and $\tau$ is the relaxation time. Besides the electron's relaxation time, the thermal conductivity is strongly and directly affected by temperature. This effect stems from the electron heat capacity in the thermal conductivity relation. The heat capacity is $C=\gamma T$, where γ is 3.1 $mJ \cdot mol^{-1} \cdot K^{-2}$ for Ir, when the temperature is not too high.[45] The temperature in the thermal conductivity's expression overshadows the physics behind the variation of $\kappa$ against $T$. The traditional thermal resistivity is defined as $W = \kappa^{-1} = 3/\gamma T v_F^2 \tau$. Instead of directly looking at $W$, we define a unified thermal resistivity: $\Theta = W \times T$. It is clear this unified thermal resistivity is solely related to the electron relaxation time. This unified thermal resistivity plays the same critical role as the electrical resistivity in reflecting the electron scattering in metals.

We plot out the unified thermal resistivity variation against temperature in comparison with the bulk's values,[1, 3] as depicted in figure 8. "3.2 nm" is for the Θ of 3.2 nm-thick Ir film calculated from $\Delta\alpha_{eff}$ shown in figure 6. One striking phenomenon is that the unified thermal resistivity follows a very similar trend to the behavior of electrical resistivity. When temperature is extended to 0, Θ of bulk Ir is almost 0 with a negligible residual value. For the Ir film, it has a residual value of about 5.5 $mK^2/W$ [$\Theta_0$]. This value makes the dominant contribution to the overall Θ. At room temperature, the overall Θ is only about 7 $mK^2/W$. Also the unified thermal

resistivity of the 3.2 nm thick Ir and the bulk Ir share the similar trend against temperature, although the one of 3.2 nm thick Ir has a smaller slope. When the temperature approaches zero, both reach a constant value (residual resistivity) while the Ir film has a much larger residual value. This trend similarity is totally different from that of the thermal conductivity comparison in the left inset of figure 8. In the left inset, no observable conclusion can be made about the comparison since the thermal conductivity of the Ir film and the bulk Ir shows totally different absolute values and a totally different trend of variation against temperature. Therefore, the unified thermal resistivity $\Theta$ is a critical property to reflect the electron scattering that determines thermal transport. The comparison with that of its bulk counterpart provides a great way to evaluating the effect of structural defects on electron thermal transport.

Now we can explain the completely different trend of $\kappa$ variation against $T$ for the Ir film compared with bulk Ir. The left inset shows that the thermal conductivity of bulk Ir rises sharply at low temperature. That is because the residual part of bulk Ir ($\Theta_0$) is close to zero at low temperatures. Unlike that of bulk Ir, $\Theta_0$ of the 3.2 nm-thick Ir film (about 5.5 $mK^2/W$) is much larger than the temperature dependent part $\Theta_{el\text{-}ph}$ (1.57 $mK^2/W$) at room temperature. Moreover, the effect of the temperature dependent part diminishes with decreasing temperature. This means the effect of $\Theta_0$ increases with decreasing temperature. All of these factors contribute to the decreased thermal conductivity of the Ir film when temperature decreases.

### 2.4.3 Characteristic structure size for electron scattering

Like the electrical resistivity, the classical thermal resistivity is also composed of two parts: $W = W_0 + W_{el-ph} = 3(\tau_0^{-1} + \tau_{el-ph}^{-1}) / (\gamma T v_F^2)$ . Here, subscripts "0" and "*el-ph*" represent the thermal resistivity induced by the structural imperfections and by phonon scattering respectively.

According to Matthiessen's rule and relaxation time approximation of scatterings, the unified thermal resistivity can be expressed as $\Theta = \Theta_0 + \Theta_{el-ph} = 3(\tau_0^{-1} + \tau_{el-ph}^{-1}) / (\gamma v_F^2)$. So Θ is composed of two parts: the residual part $\Theta_0$ that is temperature independent, and the temperature dependent part $\Theta_{el\text{-}ph}$. Similar to electrical resistivity, we define the slope of Θ variation against temperature as the temperature coefficient of thermal resistivity (TCTR). The TCTR of the 3.2 nm thick Ir film ($6.33\times10^{-3}$ mK/W from 290 K to 75 K) is a little smaller than, but still close to that of the bulk material ($7.62\times10^{-3}$ mK/W from 290 K to 75 K). This strongly proves they share the similar phonon-electron scattering. The unified thermal resistivity goes down with decreasing temperature due to the reduction of phonon density. This behavior is very similar to that of electrical resistivity.

The residual part of the 3.2 nm thick Ir film (about 5.5 $mK^2/W$) is much larger than that of the bulk material ($1.4\times10^{-3}$ $mK^2/W$). The Fermi energy of Ir is 0.761 R*y*.[56] The Fermi velocity can be determined as $1.91\times10^6$ m/s [$v_F = (2E_F/m_e)^{0.5}$]. Then we can obtain the value of $\tau_0$ is $3.8\times10^{-16}$ s. Finally the mean free path ($l_0$) at low temperatures is determined as 0.73 nm ($l_0=\tau_0 v_F$). At low temperatures, the effect of phonon-electron scattering diminishes. The structure scatterings, like grain boundary scattering, surface scattering and point defect scattering, dominate the electron transport. Therefore, the calculated $l_0$ gives a characteristic structure size that scatters electrons during heat conduction. The crystalline size of the thin films is estimated to be about 8 nm according to the XRD results. This size is much larger than the film thickness, proving that the film has columnar structure in the vertical direction. The size given by XRD represents the characteristic size of the columns in the lateral (in-plane) direction of the film. This is also the electron heat conduction direction studied in this work. The above revealed

nanocrystalline structure of the Ir film is confirmed by high-resolution transmission electron microscopy study.

### 2.4.4 Physical mechanism behind the observed thermal conductivity

For the characteristic size we revealed using the residual unified thermal resistivity, it includes the effect of point defect scattering, surface scattering, and grain boundary scattering as: $\tau_0^{-1} = \tau_{defect}^{-1} + \tau_{grain}^{-1} + \tau_{surface}^{-1}$ . The characterization length groups all the effects of point defect scattering, grain boundary scattering and surface scattering as $l_0^{-1} = \left(v_F \tau_{defect}\right)^{-1} + \left(v_F \tau_{grain}\right)^{-1} + \left(v_F \tau_{surface}\right)^{-1}$ . In our previous work, the weak dependence of thermal conductivity on Ir film thickness proved that the surface scattering has little effect. Rather, the grain boundary scattering plays the major role in scattering electrons. Therefore, to first order estimation, the thermal resistance relation can be written as $l_{grain}/\kappa = l_{grain}/\kappa_c + R$ . Here, $\kappa_c$ is the thermal conductivity of the bulk Ir and $R$ is the interfacial thermal resistance. Under this scenario, we can calculate the interface thermal conductance as $G = R^{-1} = (l_{grain}/\kappa - l_{grain}/\kappa_c)^{-1}$. The results are shown in figure 9 and compared with the Al/Cu interface thermal conductance. The calculated Ir/Ir thermal conductance is much larger than that of the Al/Cu interface. This is because the Al/Cu interface is more highly mismatched than the Ir/Ir interface.

The electron's specific heat is proportional to $T$ when $T$ is not too high ($=\gamma T$). The observed thermal conductance variation with temperature is mostly determined by the specific heat of electrons. To check this point, $G/T$ is also calculated and shown in the inset of figure 9. $G/T$ in fact represents a unified interface thermal conductance, and gives more direct information about the electron scattering behavior at the grain boundaries. Consequently, a unified interface

thermal resistance: *RT* can also be used for studying the electron scattering behavior at the grain boundary.

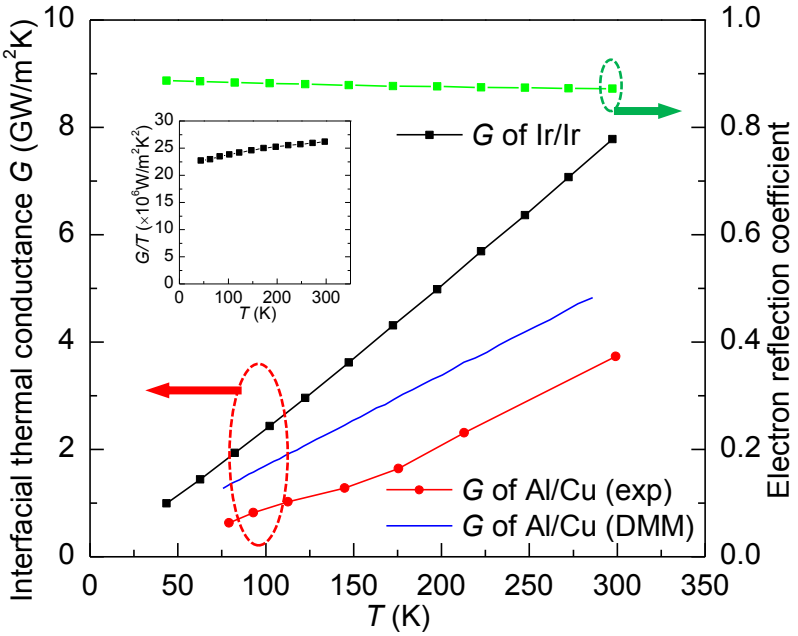


Figure 9. Temperature dependent interfacial thermal conductance and electron reflection coefficient. "*G* of Ir/Ir" is the results of this work. For comparison, "*G* of Al/Cu (exp)" is the experimental results of Al/Cu interfacial thermal conductance and "*G* of Al/Cu (DMM)" is the prediction values of Al/Cu interfacial thermal conductance according to the diffusive mismatch model (DMM).[4] The inset shows the variation of *G/T* against temperature to demonstrate that the *G*-*T* relation shown in the figure mainly comes from the electron's specific heat change against *T*.

From the inset in figure 9, we can see that *G/T* shows very weak temperature dependence. Its value changes from $2.61\times10^7$ W/m$^2$K$^2$ at room temperature to $2.27\times10^7$ W/m$^2$K$^2$ at 43 K. This indicates that interfacial thermal conductance is proportional to temperature and this temperature factor stems from the electron heat capacity. If point defect scattering is not considered and surface scattering is specular,[26, 29] this interface thermal resistance is induced

by the fact that some electrons are reflected instead of transmitting through the grain boundaries. Some reflected electrons could exchange energy with phonons at the grain boundaries before they are reflected back. Then these phonons exchange energy with phonons on the other side of the grain boundaries. In this case, the reflected electrons still have some of their energy transmitted across the grain boundaries. According to Mayadas-Shatzkes (MS) model,[50, 51] the effective electron reflection coefficient by the grain boundary can be obtained and shown in figure 9. As we can see, the electron reflection coefficient is large and almost constant. The electron reflection coefficient is 87.2% at room temperature. This means most of the electrons which scatter with the grain boundary are reflected back. This value becomes 88.7% when temperature goes down to 43 K. The very weak temperature dependent reflection coefficient indicates that the chance of electrons transport through grain boundaries is almost temperature-independent. The slightly higher grain boundary reflection coefficient at low temperatures gives rise to the slightly lower unified interface thermal conductance as indicated in the inset. It is noted that the grain boundary electron reflection coefficient we report here includes the effect of electron-phonon energy exchange adjacent to grain boundaries, and the phonon-phonon energy exchange across grain boundaries. Therefore, the real electron reflection coefficient should be a little higher than the values reported in figure 9.

## 2.5. Lorenz Number of the Ir Film

### 2.5.1. Overall Lorenz number

As we discussed above, the Lorenz number of the average 3.2 nm-thick Ir film can be determined as $L_{Lorenz}=\left(3\kappa A_2\right)/\left(\Delta GTL\right)$. $\kappa$ is the thermal conductivity of the 3.2 nm-thick Ir film. $A_2$ is the cross section area of the average 3.2 nm-thick Ir film. The length ($L$) and diameter ($d$) of

the milkweed fiber is 981 μm and 20.53 μm. *T* is the average temperature of the milkweed fiber during TET experiment. The Lorenz numbers are obtained and shown in figure 10.

Figure 10 depicts the temperature dependent Lorenz number of the average 3.2 nm-thick Ir film and the bulk Ir for comparison. Powell, *et al.* has measured the Lorenz number of the bulk Ir.[3] The electrical resistivity and thermal resistivity of the bulk Ir are given in White's paper.[1] A bulk Lorenz number calculated from their data is also shown in figure 10. The Lorenz number of the bulk Ir is a little higher than the Sommerfeld value near room temperature. This value decreases with decreasing temperature. However, the Lorenz number of the average 3.2 nm-thick Ir film shows a very different characteristic change with temperature. It is about $2.3\times10^{-8}$ $W\Omega/K^2$ near room temperature, which is a little smaller than the bulk's value and Sommerfeld value. When temperature falls down to 43 K, it remains almost unchanged.

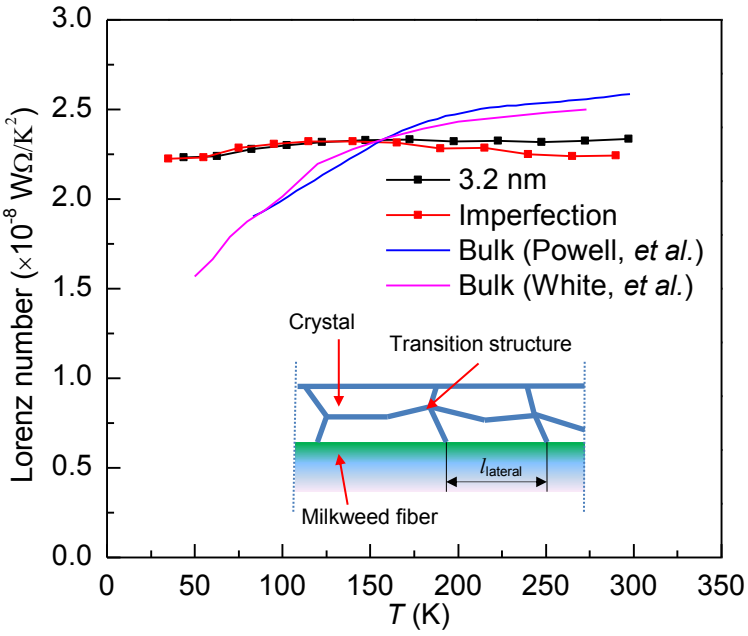


Figure 10. Temperature dependence of the Lorenz number of the 3.2 nm-thick Ir film, imperfect structure and the bulk Ir. [1, 3] The inset shows the schematic diagram of the Ir film structure.

It is well documented that $L_{Lorenz} = \kappa/(\sigma T)$ with ($\sigma$=1/$\rho$), so we have $L_{Lorenz} = \rho/\Theta$. The electron transport includes four scattering mechanisms: structural scattering, phonon scattering, phonon-assisted electron energy transfer and tunneling, hopping. If we do not consider the effect of phonon-assisted electron energy transfer, tunneling and hopping, we have

$$L_{Lorenz} = \frac{\rho}{\Theta} = \frac{\rho_0 + \rho_{el-ph}}{\Theta_0 + \Theta_{el-ph}}, \tag{9}$$

where subscripts "**0**"and "*el-ph*" represent the residual part and temperature dependent part respectively. $\rho$ and $\Theta$ are composed of the residual part and electron-phonon scattering (temperature dependent) part. For bulk material, the residual part is negligible, and the temperature dependent part dominates. Therefore, for the bulk Ir, the Lorenz number is strongly temperature dependent.

Unlike the bulk Ir, the 3.2 nm-thick Ir film's $\rho_0$($1.24\times10^{-7}\Omega\cdot$m) is much larger than the temperature dependent part ($\rho_{el\text{-}ph}$=$3.4\times10^{-8}\Omega\cdot$m) at room temperature. Similarly, $\Theta_0$ (about 5.5 $mK^2/W$) is much larger than the temperature dependent part ($\Theta_{el\text{-}ph}$=1.57$mK^2/W$) at room temperature according to figure 8. When the temperature goes down, the effect of the temperature dependent part decreases gradually and finally reaches zero. $\rho_0$ and $\Theta_0$ dominate the Lorenz number of the 3.2 nm-thick Ir film. Both of them are temperature independent. Moreover, the TCER of the 3.2 nm-thick Ir film is smaller than that of the bulk material, which indicates that the temperature-dependent part of the 3.2 nm-thick Ir film shows weaker temperature dependence than that of the bulk material. Therefore, the Lorenz number of the 3.2 nm-thick Ir film remains almost unchanged against temperature.

### 2.5.2. Lorenz number of imperfections

The 3.2 nm-thick Ir film is composed of a crystalline region and an imperfect structure, just as shown in the inset of figure 10. The film has columnar structure in the vertical direction. The thickness of the film (average 3.2 nm) is much smaller than the lateral characteristic size (about 8 nm). The imperfect structure in the film includes the extremely large surface area, grain boundary. The high resolution TEM image in figure 2(d) also confirms this. They give rise to extra electron scattering and increased $\rho$ and $\Theta$. Therefore, when we do not consider the effect of phonon-assisted electron energy transfer, tunneling and hopping, the electrical resistivity and unified thermal resistivity can be separated as below, as some addition on top of that of bulk Ir:

$$L_{Lorenz} = \frac{\rho_b + \rho_{imper}}{\Theta_b + \Theta_{imper}}, \tag{10}$$

where subscripts "b" and "imper" represent the bulk Ir value, and imperfect structures in the 3.2 nm-thick Ir film. According to the electrical resistivity and Lorenz number of the bulk crystal Ir, $\rho_b$ and $\Theta_b$ can be obtained. The overall electrical resistivity and Lorenz number are already measured in this work, so we can evaluate the electrical resistivity $\rho_{imper}$ and $\Theta_{imper}$ of the imperfect structures.

The inset of figure 10 depicts the schematic diagram of the Ir film structure. The electrical resistivity of the imperfect structure dominates the overall electrical resistivity. Its value is shown in figure 5, and has a negative temperature coefficient. This phenomenon is also observed in other amorphous metals.[57, 58] Similarly, $\Theta_{imper}$ is dominant in the overall $\Theta$, and it also has weak negative temperature dependence. Its value is displayed in figure 8. At room temperature, the unified thermal resistivity of the imperfect structure is 4.78 $mK^2/W$. It increases to 5.50 $mK^2/W$ when the temperature decreases down to about 40 K. Here, we define the Lorenz

number of the imperfect structure of Ir in the average 3.2 nm-thick Ir film as $L_{Lorenz,imper}=\rho_{imper}/\Theta_{imper}$ which is shown in figure 10. As we can see from it, the Lorenz number of the imperfect structures in the 3.2 nm-thick Ir film shows a very similar trend versus temperature like the overall Lorenz number. At high temperatures (close to room temperature), the Lorenz number of the imperfect structures is a little lower than of the overall one. This little difference results from the temperature dependent part of $\rho$ and $\Theta$. When the temperature decreases, the effect of the temperature dependent part diminishes gradually. Therefore, at lower temperatures (<150 K), it becomes the same as the overall one. The imperfect structure makes the dominant contribution to the electrical and unified thermal resistivity. These parts of the resistivity are weakly temperature dependent, and determine the overall Lorenz number and its change against temperature. Since the Lorenz number of the imperfect structure is close to the Sommerfeld value, it is conclusive that the electron scattering by the imperfect structures plays the same role in reducing charge and heat transport.

### 2.5.3. Scattering mechanism of heat and charge carriers

From the perspective of the scattering mechanism, charge currents are limited by phonon-electron scattering in conventional metals. The scatterings involving phonons with large wave vectors (larger than Fermi wave vector) are called large angle scattering. They impede the transport of the heat and charge current equally. By contrast, the scatterings involving phonons with small wave vectors (much smaller than Fermi wave vector) are called small angle scattering. The small angle scatterings relax the heat current and leave the charge current relatively unchanged.[59, 60] At high temperatures (usually higher than Debye temperature), the mean free paths for entropy and charge transport are comparable and large angle scattering is

dominant. But when temperature decreases, only small wave vector phonons are excited. The phonon population changes gradually towards the small wave vector limit. In this case, the mean free path for electron transport is relatively larger than that for entropy transport, which results in the decreased Lorenz number. When temperature is very low, the Lorenz number comes back to the Sommerfeld value and the mean free paths for entropy and electron transport are comparable again. This is because the phonons are frozen, and the dominant scattering is the elastic scattering due to structural imperfections.[60]

For the bulk Ir, the large angle scattering dominates at high temperatures so the Lorenz number is close to the Sommerfeld value and shows weak temperature dependence. At low temperatures the contribution of small angle scattering becomes dominant.[22] Due to small angle scattering, the heat current decreases while the charge current is left relatively unaffected. Therefore, the Lorenz number of the bulk Ir is reduced at low temperatures as shown in figure 10. However, for the average 3.2 nm-thick Ir film, the scattering sources are mainly grain boundary, impurities and point defects. Similar to single metallic nanowires,[22] elastic scatterings are dominant for the average 3.2 nm-thick Ir film and mostly result from grain boundaries. The mean free paths for entropy and electron transport are limited by these elastic scatterings comparably. So the Lorenz number of the average 3.2 nm-thick Ir film remains almost unchanged with temperature.

For the imperfect structure in the average 3.2 nm-thick Ir film, the entropy and electron mean free path are limited only by these imperfection scatterings. In this “metallic glass” structure (transition region between grains), the scatterings are totally elastic electron imperfection scatterings. Therefore, the Lorenz number of the imperfect structure in the average 3.2 nm-thick Ir film also remains almost unchanged with temperature. Wilson *et al.*

experimentally confirmed that the Wiedemann-Franz Law was valid for nanoscale Pd/Ir interfaces,[28] which means the heat current and electron current pass through these interfaces equally.

Here, we also confirm that the heat current and electron current transport through the imperfect structure equally and the Wiedemann-Franz Law holds. The imperfect structure dominates in the average 3.2 nm-thick Ir film. That is why the Lorenz number of the imperfect structure shares a similar trend with the overall Lorenz number. At high temperatures (close to room temperature), the Lorenz number of the imperfect structure is a little smaller than the overall one. Temperature dependent phonon scatterings contribute to this small difference. When the temperature goes down, the effect of phonon scatterings diminishes gradually and the effect of imperfect structure enlarges. That is why the Lorenz number of the imperfect structure and overall film are the same at low temperatures.

One phenomenon that should be noted is that the Lorenz number of the 3.2 nm-thick Ir film on milkweed fiber is close to the Sommerfeld value. However, all the measured Lorenz numbers of low dimensional metallic structures in the literature are larger than the Sommerfeld value. These large Lorenz numbers result from grain boundary scattering, which impedes charge transport and heat conduction to different degrees. The energy of scattered electrons can be partly transferred across the grain boundary via electron-phonon scattering because phonons can transport through the grain boundary more readily than electrons. Similar results (large Lorenz number) are also obtained for thin Ir and gold films on glass fiber at room temperature.[26, 29] Unlike the glass fiber, the Lorenz numbers of Ir and gold film on silkworm silk [61] and Ir film on milkweed fiber in this work are close to the Sommerfeld value. This bulk-like behavior of the Lorenz number is like that of metallic glass. However, the thermal conductivity ($\leq$10.6 W/mK)

and electrical conductivity ($\leq 14.2\times10^5\ \Omega^{-1}m^{-1}$) of metallic glasses are much smaller than those of Ir film on silkworm silk and milkweed fiber.[61] In our past work we have found the thermal conductivity of the same Ir film on silkworm silk is smaller or close to that on glass fiber. But the electrical conductivity of Ir film on silkworm silk is several times larger than that on glass fiber. A similar result is also observed when comparing the thermal conductivity and electrical conductivity of Ir film on milkweed fiber and glass fiber. Therefore, the observed enhanced electrical conductivity is speculated to be due to electron hopping and tunneling in the substrate material (milkweed fiber).[61] The electron hopping and tunneling in biomaterials is also observed in gold-coated and amine-functionalized carbon nanotubes-coated spider silk. Gold films on spider silk are composed of gold nanoparticles and have excellent electron transport properties. The electronic conduction in the spider silk is attributed to electron hopping and/or tunneling.[62] The charge carrier transport among amine-functionalized carbon nanotubes on spider silk is also sustained by charge hopping.[63] The electron transport via proteins is due to tunneling and hopping through the saturated molecules (linear alkane molecules) or/and conjugated molecules (π-conjugation).[64] Similarly, in lignin there are a large number of conjugated molecules (π-conjugation) and lignin is an important component of plant cell wall. Therefore, the mechanism of enhanced electrical conductivity and bulk-like Lorenz number of Ir films on milkweed fiber is speculated to be electron tunneling and hopping through lignin in the cell wall.

## 2.6. Uncertainty Analysis

The relative error of length and diameter measurement with SEM, and electrical current and electrical resistance measurement are estimated as 1% and 0.5% respectively. The relative

error of the Ir film thickness measurement is 2% determined by the quartz crystal microbalance in the sputtering system. For thermal diffusivity, every value is measured twenty times and the average value is determined as the final result. The maximum relative error for the fitting process is 10% but the real error is much smaller than 10%. Through fitting the thermal diffusivity difference ($\Delta\alpha_{eff}$), the average absolute error is $1.35\times10^{-8}$ $m^2/s$. The relative error of $\Delta\alpha_{eff}$ is then 6%. The fitting of volumetric specific heat shows a relative error of 6.4% and the volumetric specific heat is measured four times. So the relative error of average volumetric specific heat is 3.2%. Finally the relative error of the thermal conductivity of the Ir film is estimated as 7.2%.

# CHAPTER 3
# ELECTRICAL AND THERMAL CONDUCTION IN SILVER NANOWIRE

## 3.1 Overall

In this chapter, a single silver nanowire is suspended across two electrodes and Electron Beam Induced Deposition (EBID) is used to deposit Pt pads on the ends of the nanowire to suppress the electrical and thermal contact resistances. The top and side views of the suspended silver nanowire and the atom force microscope (AFM) figures of the nanowire surface are shown in figure 11. X-ray diffraction (XRD) is used to characterize the structure of the silver nanowires and the XRD pattern is shown in figure 12. More details about sample preparation and structure can be found below. The thermal and electrical properties of a single suspended silver nanowire are characterized with a steady state electro-thermal technique from room temperature down to 35 K. The temperature dependent Lorenz number is also determined. The thermal and electrical conductivities of the nanowire are compared with their bulk counterpart and a unified thermal resistivity is used to reveal the scattering mechanism.

## 3.2 Methods

### 3.2.1 Sample preparation and structure

Silver nanowires used in this work were purchased from Sigma-aldrich and they were supplied as suspensions in isopropyl alcohol (IPA) with a concentration of 0.5%. The purchased dispersion was further diluted with IPA and dropped on a piece of gel film. The silver nanowires remained on the gel film after IPA evaporated. In this process, the purchased dispersion should be diluted to a degree that single silver nanowires stayed on the gel film without contact with the surrounding ones. Then we used a very simple but effective way to make electrodes for

suspending a single nanowire. First of all, a 180 nm thick Au film was deposited on a thermal oxide silicon wafer with a 1 μm thick $SiO_2$ layer. The wafer ($Au/SiO_2/Si$) was cut into pieces and assembled into two electrodes on a glass slide. The trench width is adjustable and the minimum trench width by this method is 5 μm. If the width is smaller than 5 μm, the two electrodes would be prone to connect with each other electrically. The width used in this work was about 25 μm. The two ends of the trench were fixed to the glass slide by epoxy glue.

Before bridging the nanowire, the two electrodes were checked to make sure that they did not connect with each other electrically. After that, a probe station was used to manipulate a single silver nanowire and bridge it across the electrodes. Finally, to suppress thermal and electrical contact resistance, EBID was used to deposit Pt on the two ends of the silver nanowire. To guarantee the good thermal and electrical contact between the silver nanowire and the electrodes, the Pt pads are large and thick enough to cover the entire silver nanowire ends. For the thermal and electrical characterization of the single silver nanowire at low temperatures, a cryogenic system [CCS-450, JANIS] was used to provide cryogenic experiment environment as low as 10 K. The sample was put in a vacuum chamber to suppress the convection heat transfer. The pressure of the chamber is below 0.5 mTorr. The schematic diagram and SEM picture of the two electrodes and the silver nanowire sample (top view) are shown in figure 11(a) and (b). The side views are shown in figure 11(c) and (d). According to the top view and side view of the silver nanowire, the three dimension coordinates of the nanowire can be extracted and the length of the suspended silver nanowire is calculated as 27.23 μm. Unlike the length, the average nanowire diameter is easy to measure using SEM and its value is determined as 227 nm.

To characterize the structure of the silver nanowire, XRD was used to scan the sample. The XRD system (Siemens D 500 diffractometer) is equipped with a copper tube that was operated at 40 kV and 30 mA. Because a single silver nanowire is too small compared with the XRD spot size and cannot provide enough signals, five drops of purchased dispersion which contained plenty of silver nanowires were dropped on the XRD sample holder. The XRD pattern is shown in figure 12. The XRD pattern shows that the silver nanowire is composed of crystals. According to the pattern, the crystal size can be estimated based on the peaks. The crystal size calculated from Peak (111) is 126 nm and those sizes calculated from Peak (220) and Peak (311) are 8 nm and 21 nm respectively. All of the crystal sizes in these directions are much smaller than the diameter of the silver nanowire. This proves that the silver nanowire is polycrystalline. The grain boundaries among these nanocrystals in the silver nanowires are abundant. Also the different crystallite size determined by the peaks indicates that the crystallite in the nanowire is not cube-like or sphere-like. Instead, the crystallite is expected to be ellipsoid-like.

To study the surface roughness of silver nanowires, the AFM (MicroNano D 3000) is employed. To prepare a sample for the AFM scanning, a small amount of aqueous solution containing silver nanowires is dropped on a glass substrate. After water evaporates, the silver nanowires are dispersed on the substrate. Figure 11(e) shows the AFM image of the silver nanowires on the substrate. Then a randomly selected $160 \times 160$ nm$^2$ area is finely scanned and the surface image is shown in figure 11(f). The cross-section profiles show a fluctuation of $\pm$ 2 nm in the $z$ direction.

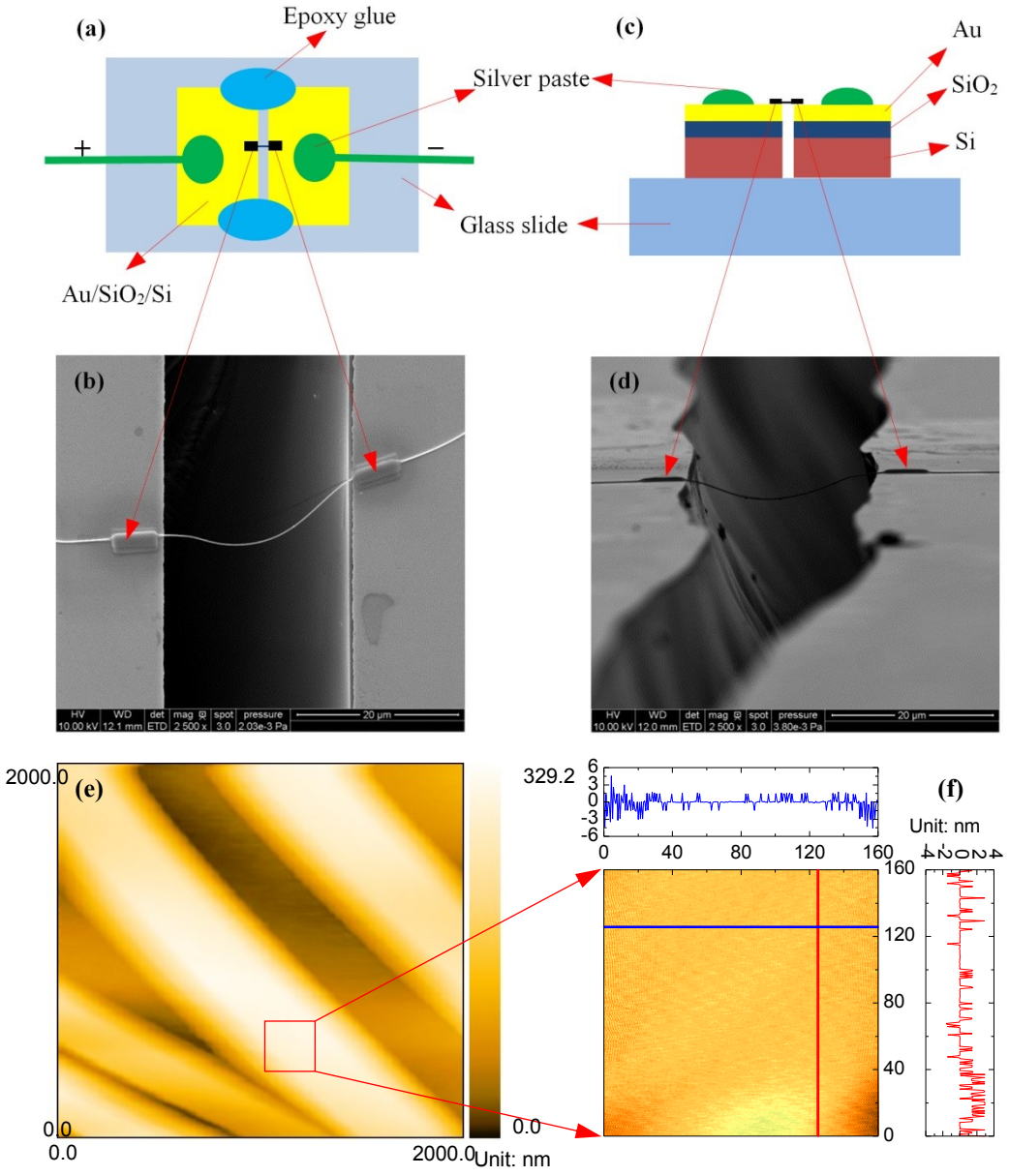


Figure 11. (a) Schematic diagram of the electrodes and the suspended silver nanowire (top view). (b) SEM picture of the electrodes and the suspended silver nanowire (top view). (c) Schematic diagram of the electrodes and the suspended silver nanowire (side view). (d) SEM picture of the electrodes and the suspended silver nanowire (side view). (e) AFM image of silver nanowires dispersed on a glass substrate for roughness measurement. (f) Finely scanned AFM image of a selected 160 × 160 $nm^2$ area indicated in (e) by red square. The cross-section profiles along the *x* (blue) and *y* (red) directions are shown on the top and right sides of the contour plot respectively.

### 3.2.2 Electrical characterization

For the electrical characterization of the silver nanowire, a set of small electrical currents ranging from 0.1 mA to 0.5 mA were applied. The current source is Keithley 6221 DC and AC Current Source. Due to the electrical heating effect, the electrical resistance would rise when the electrical current increases. The measured electrical resistance should change proportionally with the electrical current's square. A linear fitting was used to extrapolate the electrical resistance without heating effect, namely the resistance when the electrical current is zero.

### 3.2.3 Thermal characterization

The thermal conductivity of the nanowire is characterized by using the steady-state electro-thermal technique. The silver nanowire is suspended across the two electrodes in the characterization. We can consider the two electrodes as two heat sinks. Its temperature is the same as the environment temperature $T_0$. The sample is placed in a high vacuum chamber to suppress the convection effect. Moreover, the radiation effect would be small because the nanowire is very short. Also, it is well known that silver has a very small emissivity (about 0.03). Therefore, the effect of convection and radiation is negligible in this work. When a constant electrical current is applied through the nanowire, the joule self-heating in the nanowire would induce a temperature rise. The steady-state heat transfer governing equation is as below:

$$k\frac{\partial^2 T(x)}{\partial x^2}+q_0=0. \tag{11}$$

Here, $k$ is the thermal conductivity and $q_0$ is the heat generation rate per unit volume. It can be described as $q_0 = I^2 R_1 / (A_c L)$. $I$ is the applied electrical current; $R_1$ is the electrical resistance of

the nanowire; $A_c$ is the cross section area of the nanowire ( $A_c = \pi d^2/4$ ) and $L$ is the length of the nanowire. The expression of $T$(x) is $T(x) = T_0 - q_0(x^2 - xL)/(2\kappa)$. The average temperature along the sample is

$$T = \frac{1}{L}\int_{x=0}^{L} T(x)dx = T_0 + \frac{q_0 L^2}{12k}. \quad (12)$$

The temperature rise is $\Delta T = I^2 R_1 L/(12kA_c)$. As we can see, the temperature rise is proportional to electrical current's square. When the temperature is higher than 35 K, the electrical resistance of the silver nanowire is proportional to its temperature. The temperature change can be monitored by the electrical resistance variation $\Delta R$ :

$$\Delta R = \frac{dR}{dT}\Delta T = \frac{dR}{dT}\cdot\frac{I^2 R_1 L}{12kA_c}. \quad (13)$$

It can be seen from equation (13) that $\Delta R$ is proportional to $I^2$ and the slope is $slope = R_1 L\cdot(dR/dT)/(12kA_c)$. Then the thermal conductivity of the nanowire can be determined as below:

$$k = \frac{dR}{dT}\cdot\frac{R_1 L}{12A_c\cdot slope}. \quad (14)$$

Now we take the thermal conductivity characterization of the silver nanowire at 290 K as an example to demonstrate the measurement process. At first, a series of electrical currents ranging from 0.1 mA to 0.5 mA were applied through the sample and the corresponding voltages were measured by a digit multimeter (Agilent 34401A). Then we plot the relation between the electrical resistance and the current's square as shown in the inset of figure 14. After fitting the data linearly, the slope (1.83 Ω/mA$^2$) and intercept (53.15 Ω) can be obtained. The intercept is the electrical resistance ($R_0$) at 290 K. After we measured the electrical resistances at different

temperatures, the value of $dR/dT$ (0.1165 Ω/K) can be determined. The diameter and length of the silver nanowire were measured by a scanning electron microscopy (SEM) after the experiment was finished. Finally, the thermal conductivity of the silver nanowire was determined as 191.5 W/K·m. In order to improve the measurement accuracy, the electrical resistance rise induced in all the experiments was carefully selected as about 1%. The temperature rises were all controlled within 5 K.

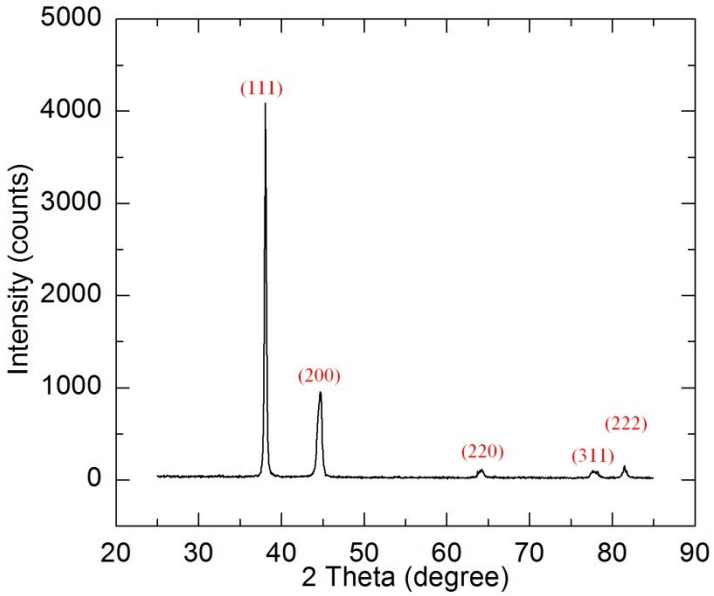


Figure 12. XRD pattern of the silver nanowires. According to the XRD results, the lattice plane spacing for peaks (111), (220) and (311) are 2.3616 Å, 1.4518 Å and 1.2287 Å respectively. The corresponding lattice constant can be calculated as 4.09 Å, 4.11 Å and 4.08 Å for the nanowire in our work. The lattice constant of bulk silver is 4.09 Å. This confirms the FCC structure of silver crystal.

## 3.3 Electrical Conduction in Single Silver Nanowire

A set of small electrical currents ranging from 0.1 mA to 0.5 mA were applied to the sample. The corresponding voltages can be measured. Then the electrical resistance can be

obtained. The electrical resistance without joule heating can be obtained by linear fitting and extrapolation. After knowing the geometrical sizes of the films, the electrical resistivity can be calculated. The temperature dependent electrical resistivity is shown in figure 13 and fitted with the Bloch-Grüneisen formula. For comparison, the temperature dependent electrical resistivity of bulk silver is also shown in figure 13 and fitted with the Bloch-Grüneisen formula. [5] Additionally, the electrical resistance of the silver nanowire is also shown in figure 13 with the right coordinate. According to the Matthiessen's rule and the Bloch-Grüneisen theory,[43] the electrical resistivity can be expressed as $\rho=\rho_0+\rho_{el-ph}$. $\rho_0$ is the residual resistivity which results from structural scatterings, like grain boundary scattering, impurity scattering and surface scattering. It is essentially temperature independent and its value is the electrical resistivity when the temperature approaches zero. $\rho_{el-ph}$ is the temperature dependent electrical resistivity induced by phonon scattering, and can be expressed as

$$\rho_{el-ph} = \alpha_{el-ph}\left(\frac{T}{\theta}\right)^n \int_0^{\theta/T} \frac{x^n}{\left(e^x-1\right)\left(1-e^{-x}\right)}dx, \tag{15}$$

where $\alpha_{el-ph}$ is the electron-phonon coupling parameter. $\theta$ is the Debye temperature and $n$ generally takes the value of 5 for nonmagnetic metals.[20] Through fitting the experimental data, the Debye temperature and the electron-phonon coupling constant can be obtained respectively. The Debye temperature of the silver nanowire and the bulk silver is 151 K and 235 K and the electron-phonon coupling constant of the silver nanowire and the bulk silver is $9.90\times10^{-8}$ Ω·m and $5.24\times10^{-8}$ Ω·m. The excellent fitting curves indicate that the phonon-electron scattering dominates the temperature dependent part of the electrical resistivity. The large electron-phonon coupling constant of the silver nanowire indicates the enhanced electron-phonon coupling, which is also observed in ultrathin copper film due to surface roughness.[65] In this work, the surface

of nanowires is scanned by an atomic force microscope. The results show that the surface roughness is ± 2 nm. This surface roughness combined with internal surfaces, like grain boundaries, is responsible for the enhanced electron-phonon coupling.

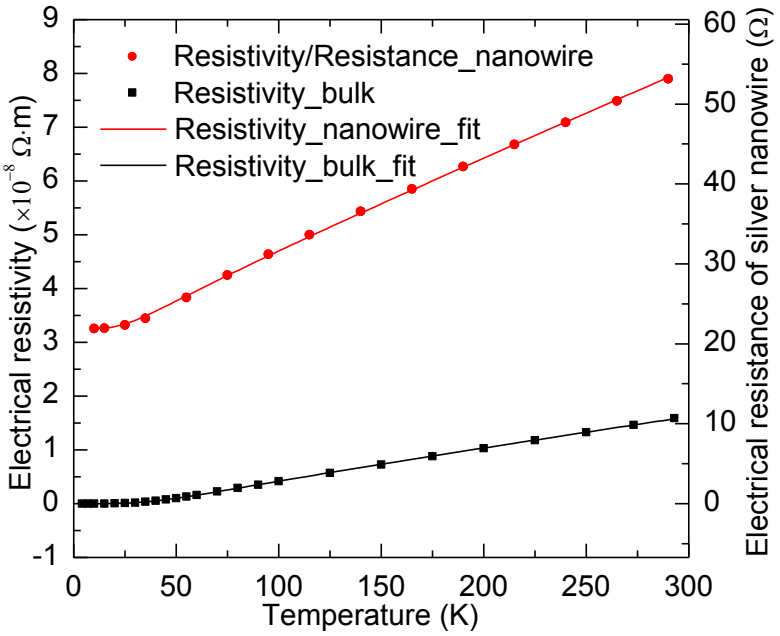


Figure 13. Temperature dependent electrical resistivity of the silver nanowire and the bulk silver.[5] They are fitted with the Bloch-Grüneisen formula. The temperature dependent electrical resistance of the silver nanowire is also shown with the right coordinate.

We can see from figure 13 that the residual electrical resistivity of the bulk silver is almost zero ($1\times10^{-11}$ Ω·m) while that of the silver nanowire is much larger ($3.25\times10^{-8}$ Ω·m). The electrical resistivity of silver nanowire at low temperatures is more than three orders of magnitude larger than that of the bulk silver. This is due to the intensive structural electron scatterings like grain boundary scattering and surface scattering. Because at low temperatures the phonon scattering diminishes, only structural scatterings contribute to impeding electron transport. The electrical resistivity of silver nanowire at room temperature is five times as large

as the counterpart of the bulk silver. This is due to the combined effect of different structural and phonon scatterings. For bulk silver, the phonon-electron scattering dominates at room temperature. But for the silver nanowire, both the phonon scattering and structural scatterings contribute to the large electrical resistivity.

It can be seen from figure 13 that the electrical resistivity changes linearly with temperature when temperature is not very low. The slope of the silver nanowire's electrical resistivity against temperature ($1.68\times10^{-10}$ Ω·m/K) is much larger than that of the bulk silver ($6.11\times10^{-11}$ Ω·m/K). Similar phenomenon is also observed in Co/Ni Superlattices.[46] Furthermore, the electrical resistivity of the silver nanowire and the bulk silver are both fitted well with the Bloch-Grüneisen theory. The fitting results show that the Debye temperature of the silver nanowire (151 K) is much smaller than that of the bulk silver (235 K). The reduced Debye temperature is due to surface phonon softening. The missing bonds of atoms at the surfaces, including inner surfaces like grain boundaries, lead to the change of phonon modes and vibration frequency. These changes result in the reduced Debye temperature. [18, 19, 46-48] To conclude, the enhanced electron-phonon coupling and the reduced Debye temperature result in the large slope of electrical resistivity versus temperature.

The electrical conductivity of silver is $\rho = m\tau^{-1}/\left(ne^2\right)$. Here, $m$ and $e$ is the electron mass and charge; $\tau$ is the relaxation time and $n$ is the electron density. When the temperature approaches zero, the effect of phonon scattering would diminish and the structural scatterings dominate in electron transport. The residual resistivity can be written as $\rho_0 = m\tau_0^{-1}/\left(ne^2\right)$. The electron density of silver is $5.85\times10^{28}$ $m^{-3}$.[45] The relaxation time is $\tau_0 = 1.87\times10^{-14}$ s. The Fermi velocity of silver is $1.39\times10^{6}$ m/s. [45] So the electron mean free path induced by the structural scatterings based on the residual electrical resistivity is 26 nm. This characterization

length is close to the crystal size (21 nm) in the direction (311). The electron transport direction in our work is along the axial direction of the silver nanowire, we can conclude that axial direction is along (311).

## 3.4 Thermal Conduction in Single Silver Nanowire

When applying different electrical currents, the nanowire temperature would change due to the joule heating. The temperature change would induce electrical resistance variation. After building a heat transfer model, the thermal conductivity can be inferred based on the relation between the applied currents and the resistances. The measured temperature dependent thermal conductivity of the silver nanowire is shown and compared with bulk values in figure 14. As we can see from figure 14, the thermal conductivity of the silver nanowire at 290 K is reduced by 55% from the corresponding bulk's value. Apart from the phonon-electron scattering similar to that in the bulk silver, the extensive structural scatterings, like grain boundary and surface scatterings, also contribute to this reduction. These scatterings limit the electron mean free path and subsequently lead to the reduced thermal conductivity. The measured thermal conductivity of single silver nanowire is close to the value in reference [66]. As the temperature decreases, the thermal conductivity of the silver nanowire behaves totally different from the bulk counterpart. The thermal conductivity of the silver nanowire decreases with decreasing temperature while that of the bulk silver increases with decreasing temperature. Specifically, for bulk silver, the thermal conductivity increases more than ten times when the temperature goes down to 20 K. But for the silver nanowire, the thermal conductivity decreases by 79% when the temperature decreases to 35 K. It is notable that at low temperatures, almost two orders of magnitude reduction in the thermal conductivity was observed for the silver nanowire compared with the bulk silver.

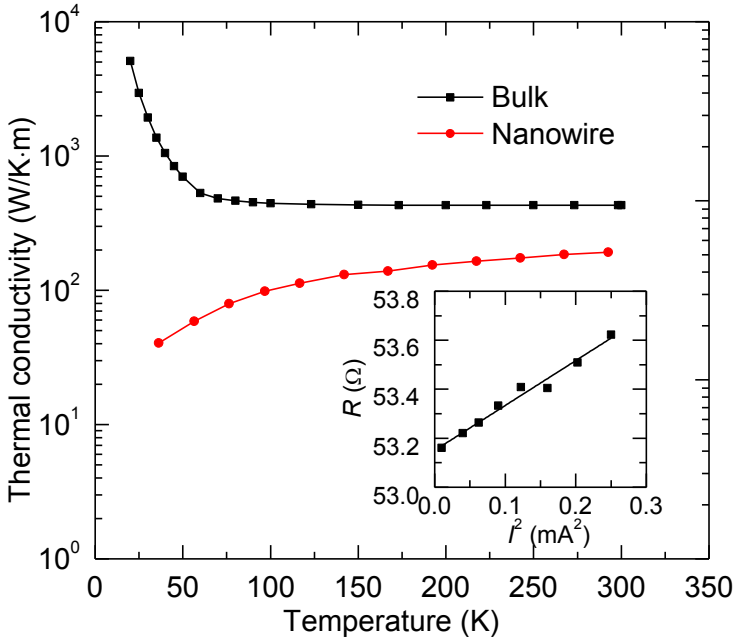


Figure 14. Temperature dependent thermal conductivity of the silver nanowire and the bulk silver.[6] The lines connecting the experimental data are just used to guide the eyes. The inset shows the linear relation between the electrical resistance and the electrical current's square at 290 K during the thermal conductivity measurement of the silver nanowire. The fitting line is $R = 53.15+1.833\times I^2$.

For bulk silver, structural scatterings are rare and phonon scattering dominates the electron transport. When temperature goes down, the short wave phonons are frozen out. The number of excited phonons which involves phonon-electron scattering decreases with decreasing temperature. That is why the thermal conductivity of the bulk silver increases with decreasing temperature. But for the silver nanowire, both structural scatterings and phonon scattering play important roles in the electron transport. When temperature goes down, the phonon scattering diminishes but the structural scatterings still exist and dominate the electron transport. Moreover, the heat capacity of electrons decreases linearly with temperature when the temperature is not too high. That is why the thermal conductivity of the silver nanowire decreases with decreasing

temperature. This phenomenon has also been observed in nickel nanowire,[22] gold and platinum nanofilms [10, 53, 54] and alloys [55].

Here an explanation is provided to the abnormal temperature dependent thermal conductivity of these nanostructures. The thermal conductivity can be written as $\kappa = C_v v_F^2 \tau / 3$. Here $C_v$ is the electron volumetric heat capacity; $v_F$ is the Fermi velocity and $\tau$ is the relaxation time. The volumetric heat capacity of electrons changes linearly with temperature when temperature is not too high ($C_v = \gamma T$). Here $\gamma$ is a constant (0.646 mJ·mol$^{-1}$·K$^{-2}$ for silver). The Fermi velocity of silver is $1.39\times10^6$ m/s and its electron density is $5.85\times10^{28}$ m$^{-3}$.[45] The temperature in the electron heat capacity overshadows the physics of the scattering mechanism behind the variation of thermal conductivity against temperature. Instead of using the traditional thermal resistivity, here we use a unified thermal resistivity $\Theta = T/\kappa$ to explain the thermal conductivity of the nanostructures. The unified thermal resistivity is solely related to the electron relaxation time as below:

$$\Theta = \frac{3}{\gamma v_F^2} \cdot \tau^{-1}. \tag{16}$$

According to the Matthiessen's rule, the unified thermal diffusivity can be separated as two parts: the phonon scattering part and the structural scattering part as below:

$$\Theta = \frac{3}{\gamma v_F^2} \cdot \tau_0^{-1} + \frac{3}{\gamma v_F^2} \cdot \tau_{ph}^{-1} = \Theta_0 + \Theta_{ph}. \tag{17}$$

Getting rid of the effect of temperature on thermal resistivity due to the electron heat capacity, the unified thermal resistivity extracts the effect of temperature on the electron scattering mechanism. The temperature dependent unified thermal resistivity of the silver nanowire and the bulk silver are depicted in figure 15. As we can see, the unified thermal resistivity of the silver

nanowire ($\Theta_{nanowire}$) and the bulk silver ($\Theta_{bulk}$) shares the same trend when changing against temperature. The two lines are parallel when temperature is not too low. When temperature is above 60 K, the slope of silver nanowire's unified thermal resistivity variation against temperature is $2.57\times10^{-3}$ m·K/W and that of the bulk silver is $2.41\times10^{-3}$ m·K/W. The slopes are almost the same. This is because the number of excited phonons changes linearly with temperature when temperature is not too low. This confirms that the silver nanowire and the bulk silver share the similar phonon-electron scattering mechanism ($\Theta_{ph}$) but have different structural scatterings ($\Theta_0$). The different structural scatterings lead to different residual values ($\Theta_0$) of the unified thermal resistivity. For the bulk silver, the residual unified thermal resistivity is almost zero because the structural imperfection is almost zero in the bulk silver. For the silver nanowire, the residual unified thermal resistivity is large due to grain boundary and surface scatterings which are temperature independent. This residual thermal resistivity can be used to characterize the structure of the silver nanowire because the phonons are frozen out when the temperature approaches zero. At low temperatures, the dominated structural scatterings are temperature independent. So similar to the electrical resistivity, the residual thermal resistivity is weak temperature dependent at low temperatures. This trend is confirmed by the bulk silver thermal resistivity values. So we can estimate the residual thermal resistivity by using the value at 30 K. According to the residual thermal resistivity (0.9 m·K$^2$/W), the relaxation time $\tau_0 = 3/(\gamma v_F^2 \Theta_0)$ is about $2.77\times10^{-14}$ s and the characterization length ($l_0 = v_F \tau_0$) is 38.5 nm. This characterization length (electron mean free path limited by structural imperfection) includes the effect of phonon-mediated electron energy transfer across the grain boundaries. It is larger than the real structural size of the crystals in the silver nanowire.

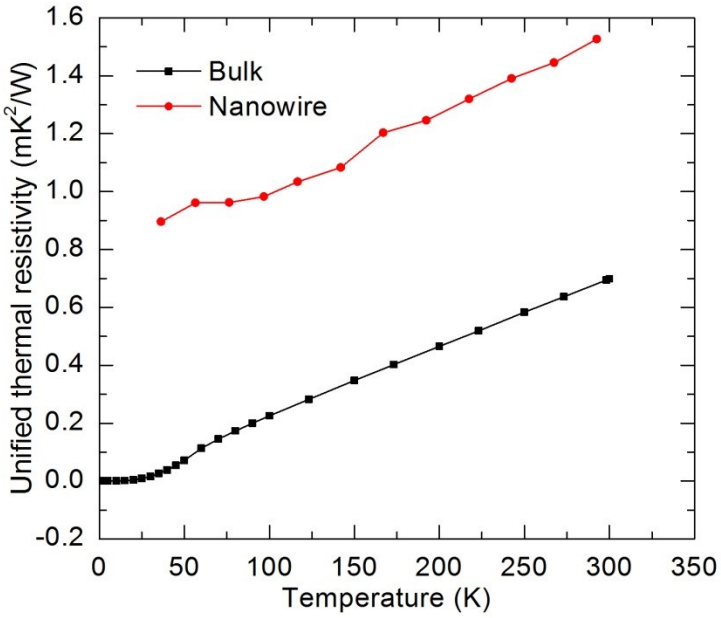


Figure 15. Temperature dependent unified thermal resistivity of the silver nanowire and the bulk silver.[6] When temperature is above 60 K, the slope of silver nanowire's unified thermal resistivity variation against temperature is $2.57\times10^{-3}$ m·K/W and that for the bulk silver is $2.41\times10^{-3}$ m·K/W.

One phenomenon which should be noticed is that, for silver nanowire, the slope of electrical resistivity variation against temperature is very different from its bulk counterpart. But the slope of Θ against temperature is almost the same as bulk silver. The same phonon scattering mechanism results in different influences on the electrical and thermal transport properties. For Ir films coated on milkweed floss, we have observed that the $\partial\Theta/\partial T$ and $\partial\rho_e/\partial T$ of Ir film show the very similar deviation from bulk Ir.[67, 68] Possible reasons for the very large difference in the thermal and electrical conduction of silver nanowire are the change of electron-phonon coupling strength induced by structural disorder and quantum size effect, and the change of phonon population and electronic structure which involves small and large angle scatterings.[69, 70] Due to the small size of the nanocrystals in the silver nanowire, the surface-to-volume ratio is large

and the quantum size effect is becoming important. The lower coordination and unsatisfied bonds of the surface atoms lead to phonon softening and the change of the electronic structure. The phonon modes of metallic nanocrystals are discretized, resulting in the change of the coupling channels of electron-phonon interactions.[69] Due to the electron wave function confinement, the electronic states are discrete. The density of states and electron density near the Fermi level decrease. The discreteness of electron energy levels would also lead to the change of electron-phonon coupling strength.[70] This is confirmed by the large electron-phonon coupling constant obtained by the Bloch-Grüneisen fitting of the electrical resistivity of the silver nanowire. These changes lead to the different responses of electrical and thermal transport to the phonon scattering.

For pure metals, it is well documented that the lattice contribution to the total thermal conductivity is negligible. [9] But for the silver nanowire in this work, the total thermal conductivity at low temperatures is very small. The phonon contribution would be significant. Here we take the case at 36 K as an example to estimate the upper limit of the lattice thermal conductivity. The specific heat of silver at 36 K is 64.65 J/(kg·K) and the density is $10.49\times10^3$ kg/m$^3$.[71] The sound speed (2600 m/s) is used to estimate the phonon velocity of silver. [52] At low temperatures, the phonon-phonon scattering mean free path becomes very long due to the decreased phonon density. Moreover, the N-process dominates the phonon-phonon scattering which does not impede heat flux directly and makes little contribution to thermal resistivity. Therefore, at low temperatures the phonon mean free path is limited by the grain boundaries (21 nm). So the upper limit of the thermal conductivity ($\kappa = C_{ph,v} v l / 3$) is calculated as 12.3 W/K·m at 36 K. The phonon mean free path should be smaller than 21 nm because other scatterings like electron-phonon scattering and point defect phonon scattering would also limit the phonon mean

free path. The real phonon thermal conductivity should be smaller than 12.3 W/K·m at 36 K. Our measured thermal conductivity is 40.46 W/K·m, so the phonon contribution to the total thermal conductivity is significant, but the electronic thermal conductivity is still dominant at low temperatures.

## 3.5 Temperature Dependent Lorenz Number of Single Silver Nanowire

After the electrical resistivity and thermal conductivity were obtained, it is ready to calculate the Lorenz number. But the measured electrical resistivity is at $T_0$ (the temperature without joule heating) while the measured thermal conductivity is at $T_{ave}$ (the average temperature during joule heating $T_{ave}= (T_0+ T_1)/2$, $T_1$ is the highest temperature with joule heating). Even though the temperature rise in the measurement process, namely the difference between $T_0$ and $T_1$, is very small (less than 5 K), we cannot calculate the Lorenz number directly. Therefore, linear interpolation was used to obtain the electrical resistivity at $T_{ave}$. Then the Lorenz number at $T_{ave}$ was determined as $L_{Lorenz} = \kappa\rho/T_{ave}$. Similarly, the Lorenz number at every $T_{ave}$ can be determined and the temperature dependent Lorenz numbers are shown in figure 16.

As we can see from figure 16, the Lorenz number at 292 K ($5.2\times10^{-8}$ $\Omega\cdot W/K^2$) is much larger than the Sommerfeld value ($2.44\times10^{-8}$ $\Omega\cdot W/K^2$). Large Lorenz numbers are also observed for nickel nanowire, gold, platinum and Iridium nanfilms. [10-12, 22, 26, 27, 29] This is due to the phonon-assisted electron energy transfer across the grain boundaries. These nanostructures are composed of nanocrystals and there are large number of grain boundaries and surfaces among them. Part of electrons would be reflected back when scattered at the grain boundaries. The reflected electrons can exchange energy with the local phonons. Phonons can transfer across the grain boundaries more readily than electrons. After phonons transfer across the grain

boundaries, they can exchange energy with the electrons and phonons in the other side of the grain boundaries. Therefore, when the electrons are reflected back, the charges do not transport through the grain boundaries but part of the electron energy transfers through the grain boundaries. This leads to the greatly reduced electrical conductivity and lesser reduced thermal conductivity.

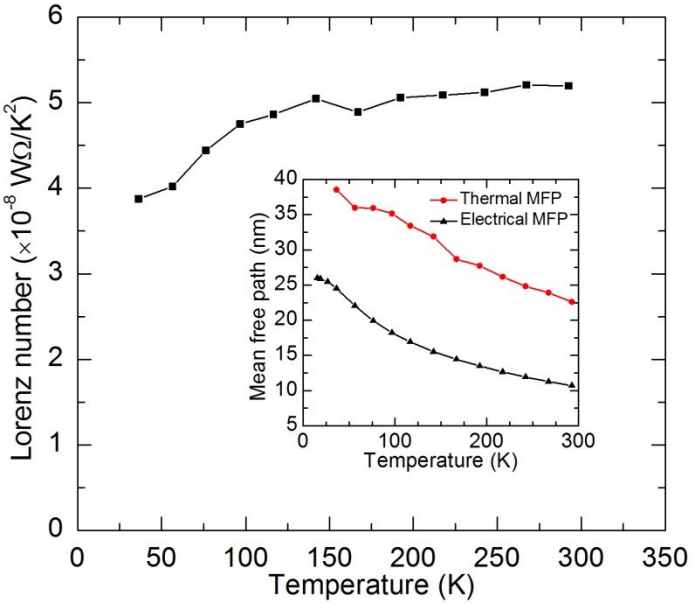


Figure 16. Temperature dependent Lorenz number of the silver nanowire. The inset shows the temperature dependent thermal and electrical electron mean free paths.

According to figure 16, the Lorenz number of the silver nanowire decreases with decreasing temperature, especially at low temperatures. This is due to the decreasing number of excited phonons and the small angle scattering. On one hand, as the temperature goes down, the number of excited phonons drops. This leads to the decreasing number of phonons which are used to assist to transfer electron energy. Consequently, the Lorenz number at reduced temperature would become smaller than the one at room temperature. On the other hand, as the temperature goes down, only phonons with small wave vector are excited. The wave vector of

the phonon population turns gradually towards the lower limit. The electron-phonon scattering would change due to the change of phonon wave vector. Electrons scattering with phonons with large wave vectors are called large angle scattering while electrons scattering with phonons with small wave vectors are called small angle scattering. Large angle scattering impedes the heat and charge transport equally while small angle scattering inhibits the heat transport significantly and leave the charge transport relatively unchanged. [22, 59, 60] At low temperatures, the Lorenz number of the silver nanowire would also decrease due to the extensive small angle scattering.

The electrical and thermal electron mean free paths shown in the inset of figure 16 can be used to interpret the Lorenz number of the silver nanowire. Because free electron model applies to silver, the electrical electron mean free path is calculated from the electrical resistivity ( $l = v_F m / (ne^2 \rho)$, $v_F$ is the Fermi velocity of silver, $m$ the electron mass, $n$ the electron density of silver and $\rho$ the electrical resistivity). Also, the thermal electron mean free path is calculated from the thermal conductivity [$l = 3\kappa / (\gamma T v_F)$ or $l = 3m\kappa v_F / (\pi^2 n k_B^2 T)$]. As we can see from the inset of figure 16, both the electrical and thermal electron mean free path increase with decreasing temperature. This is due to the reduced number of excited phonons and subsequently reduced electron-phonon scattering. The reduced scattering sources extend the electron mean free path. When the temperature approaches absolute zero, all phonons are frozen out. The phonons would not scatter electrons. The only scattering source is structural scatterings, like grain boundary, surface and point defects and these structural scatterings are temperature independent. So the electron mean free path at extremely low temperatures can reflect the structural information of the crystal structure of the silver nanowire. Here the electrical electron mean free path at extremely low temperatures is about 26 nm. This value is consistent with the crystal size (21 nm) in the direction (311) according to the XRD pattern. For the thermal electron mean free path, its

value is larger than the electrical mean free path. That is because this value includes the contribution of the phonon-assisted electron energy transfer through the grain boundaries. The difference between the electrical and thermal electron mean free path results in the large Lorenz number. Even though in this work we do not measure the thermal conductivity down to zero, it is predictable that the thermal and electrical mean free path would become the same when temperature approaches the absolute zero. The Lorenz number would become the Sommerfeld value at absolute zero. The uncertainty analysis of this work can be found the supplementary information.

## 3.6 Uncertainty Analysis

There are a few factors in the experiment which would affect the accuracy of the measurement results. Here we will have a discussion about them. First, the electrical contact resistance between the silver nanowire and the electrodes is estimated. The Pt pads deposited by EBID are large and good enough to keep good electrical contact. We conducted experiments on silver nanowire without EBID and silver nanowire with silver paste-enhanced contact. In both circumstances, to achieve 1% electrical resistance rise, the applied electrical currents increased after decreasing as the temperature went down. That is because the electrical contact resistance is weakly temperature dependent and the contact resistance dominates the total electrical resistance at low temperatures. The intrinsic electrical resistance needs to rise far more than 1% at low temperatures. That is why large electrical currents are needed at low temperatures. Here the low temperatures means above 25 K because the electrical resistivity becomes weakly temperature dependent when temperature is below 25 K. This would also lead to large applied electrical current to achieve 1% electrical resistance rise. But for the silver nanowire with EBID, the

needed electrical currents to achieve 1% resistance rise did not increase at low temperatures. The electrical contact resistance between deposited film and Pt nanowire is also reported negligible in the literature.[23] For the thermal contact resistance after EBID, the Pt-EBID has a contact conductance ($h_{con}$) of 170.5 MW/(K·m$^2$) at 293 K.[72] The Pt pad is about 5 μm long for each end and the diameter of the silver nanowire is 227 nm. So the contact area ($A_{con}$) is 1.78 μm$^2$ per end and the thermal contact resistance [$1/(A_{con}h_{con})$] between the silver nanowire and Pt pads is $3.3\times10^3$ K/W per end. The two thermal contact resistances are in parallel so the total thermal contact resistance is $1.65\times10^3$ K/W. For the silver nanowire, the effective thermal resistance is $\Delta T/q = L/(12\kappa A_c)$. This thermal resistance is defined using the average temperature rise of the sample and the total heat flux through the sample (the joule heat generated by the sample). Here, $L$ and $A_c$ is the silver nanowire length and cross section area. $\kappa$ is the thermal conductivity of the silver nanowire. The thermal resistance of the silver nanowire is $2.9\times10^5$ K/W at room temperature. The thermal contact resistance is very small compared with the thermal resistance of the silver nanowire. So the thermal contact resistance is negligible in this work. The thermal contact resistance is also reported negligible in the literature. [23, 72] The length and diameter of the silver nanowire were measured by SEM. The relative errors of the length and diameter measurement are estimated as 1% and 3% respectively. The current error is 0.5% and the voltage error is 0.3%. The relative error of the thermal conductivity and the electrical resistivity are estimated as 7.4% and 4.4% respectively.

# CHAPTER 4
# CONCLUSIONS

In this work, the thermal conductivity of bio-supported average 3.2 nm-thin Ir film was characterized for the first time from room temperature to 43 K. Close to two orders of magnitude reduction was observed for $\kappa$ of the film at low temperatures. $\kappa$ of the film increased with increasing temperature while that of bulk Ir decreased against temperature. We introduced a unified thermal resistivity ($\Theta$) to explain the completely different $\kappa$~$T$ relation of the 3.2 nm film and the bulk Ir. It was found that the 3.2 nm film and the bulk Ir share the similar trend for $\Theta$~$T$ relation. At 0 K limit, the bulk Ir has a zero residual $\Theta$ while the 3.2 nm film has a very large residual $\Theta$ (5.5 $mK^2/W$), which dominated the overall unified thermal resistivity. The unified thermal resistivity played a critical role in quantitatively explaining the effect of defect in scattering electron during heat conduction. The evaluated interfacial thermal conductance among the grain boundaries was larger than that of the Al/Cu interface. It was proportional to temperature, and this relation was confirmed by the weak temperature dependent unified interfacial thermal conductance. It was found that the electron reflection coefficient was large (88%) and almost temperature independent. For the electrical resistivity ($\rho$) of the Ir film, the extremely confined domain in the film gave a more than two-fold increase of $\rho$ from that of the bulk Ir, while they shared the similar $\rho$~$T$ trend. The $\rho$~$T$ relation was explained quantitatively by the Bloch-Grüneisen formula, and a reduced Debye temperature was obtained (~30% reduction from the bulk's value: 308 K). This phonon softening quantitatively confirmed the extensive surface and grain boundary electron scattering. More than one order of magnitude reduction was observed for the thermal conductivity of the average 3.2 nm-thick film. The Wiedemann-Franz Law still held even at low temperatures due to the large $T$-independent

residual resistivity of the ultra-thin film. The Lorenz number of the imperfect structure in the film was also evaluated. The overall Lorenz number and that of the imperfect structure (~$2.25\times10^{-8}$ $W\cdot\Omega/K^2$) were close to the Sommerfeld value and varied little against *T*. This is very much different from other low dimensional metallic structures in the literature that have a significantly increased Lorenz number. This phenomenon was speculated to be due to electron tunneling and hopping in the biomaterial substrate (lignin in this work), which helped improve electrical conduction, but left very little effect on heat conduction.

For the individual silver nanowire, its thermal and electrical transport properties were characterized down to 35 K. The results indicated that the thermal and electrical conductivities were significantly reduced compared with their bulk counterparts. The Debye temperature of the silver nanowire (151 K) is 36% lower than that of bulk silver due to phonon softening. The thermal conductivity of the silver nanowire decreased with decreasing temperature while that of the bulk silver increased. To explain these different trends, a unified thermal resistivity was used to distinguish the electron-phonon scattering and defect-electron scattering. A large residual unified thermal resistivity (0.9 $m\cdot K^2/W$) was observed for the silver nanowire. It quantifies the defect-electron scattering effect. For bulk silver, the residual unified thermal resistivity is almost zero, reflecting the relatively low defect level inside. The unified thermal resistivity changed linearly with temperature when the temperature was not too low. This is because the number of the excited phonons decreased linearly with temperature in this temperature range. The unified thermal resistivity of the silver nanowire and the bulk silver shared the same trend, proposing that the silver nanowire and the bulk silver shared the same phonon-electron scattering. Additionally, due to phonon-assisted electron energy transfer across the grain boundaries, the Lorenz number of the silver nanowire ($5.20\times10^{-8}$ $\Omega\cdot W/K^2$) was found much larger than the bulk

counterpart ($2.32\times10^{-8}$ $\Omega\cdot W/K^2$). Its value decreased with decreasing temperature due to the reduced number of the excited phonons and small angle scattering.

# CHAPTER 5
# FUTURE WORK

This work studied the electrical and thermal properties of Ir nanofilm and single silver nanowire at reduced temperatures. In the experiments, there are a lot of variables which would affect the electron transport in the metallic nanofilm, for instance, the film thickness, the substrate, the metals, deposition methods. These effects can be explored in the future and can be used to make the electrical and thermal properties tunable. For example, in this work, sputtering coating is used to deposit the Ir film. Other deposition methods, like E-Beam and thermal evaporation, also can be used to deposit the nanofilms. Different nanofilms deposited by different methods would have different structures. This would lead to different properties of the nanofilms. For the silver nanowire, self-assembled silver nanowire network can be used to explore the contact resistance. The contact resistance can be used to make the network's properties tunable. The contact resistance can be changed by adding PVP or silver nanoparticle. Subsequently, the electrical and thermal properties of silver nanowire network can be tailored as needed. Additionally, other nanoscale building blocks can be self-assembled as networks to meet different needs.

# REFERENCES


1. White, G.K. and S.B. Woods, *Electrical and Thermal Resistivity of the Transition Elements at Low Temperatures.* Philosophical Transactions of the Royal Society of London Series a-Mathematical and Physical Sciences, 1959. **251**(995): p. 273-302.
2. Blokhin, A.V., et al., *Thermodynamic Properties of Plant Biomass Components. Heat Capacity, Combustion Energy, and Gasification Equilibria of Cellulose.* Journal of Chemical and Engineering Data, 2011. **56**(9): p. 3523-3531.
3. Powell, R.W., R.P. Tye, and M.J. Woodman, *Thermal conductivities and electrical resistivities of the platinum metals.* Platinum Metals Review, 1962. **6**(4): p. 6.
4. Gundrum, B.C., D.G. Cahill, and R.S. Averback, *Thermal conductance of metal-metal interfaces.* Physical Review B, 2005. **72**(24).
5. Matula, R.A., *Electrical resistivity of copper, gold, palladium, and silver.* Journal of Physical and Chemical Reference Data, 1979. **8**(4): p. 1147-1298.
6. Ho, C.Y., R.W. Powell, and P.E. Liley, *Thermal Conductivity of the Elements: A Comprehensive Review.* Journal of Physical and Chemical Reference Data, 1974. **3**.
7. Craighead, H.G., *Nanoelectromechanical systems.* Science, 2000. **290**(5496): p. 1532-1535.
8. Chen, G., *Nanoscale energy transport and conversion : a parallel treatment of electrons, molecules, phonons, and photons*. MIT-Pappalardo series in mechanical engineering. 2005, Oxford ; New York: Oxford University Press. xxiii, 531 p.
9. Tritt, T.M., ed. *Thermal conductivity*. 2005, Kluwer Acad./Plenum Publ.
10. Yoneoka, S., et al., *Electrical and Thermal Conduction in Atomic Layer Deposition Nanobridges Down to 7 nm Thickness.* Nano Letters, 2012. **12**(2): p. 683-686.

11. Wang, H.D., et al., *Breakdown of Wiedemann-Franz law in individual suspended polycrystalline gold nanofilms down to 3 K.* International Journal of Heat and Mass Transfer, 2013. **66**: p. 585-591.
12. Wang, H.D., et al., *Experimental study on the influences of grain boundary scattering on the charge and heat transport in gold and platinum nanofilms.* Heat and Mass Transfer, 2011. **47**(8): p. 893-898.
13. De, S., et al., *Silver Nanowire Networks as Flexible, Transparent, Conducting Films: Extremely High DC to Optical Conductivity Ratios.* Acs Nano, 2009. **3**(7): p. 1767-1774.
14. Hu, L.B., et al., *Scalable Coating and Properties of Transparent, Flexible, Silver Nanowire Electrodes.* Acs Nano, 2010. **4**(5): p. 2955-2963.
15. Yang, L.Q., et al., *Solution-Processed Flexible Polymer Solar Cells with Silver Nanowire Electrodes.* ACS applied materials & interfaces, 2011. **3**(10): p. 4075-4084.
16. Yu, Z.B., et al., *Highly Flexible Silver Nanowire Electrodes for Shape-Memory Polymer Light-Emitting Diodes.* Advanced Materials, 2011. **23**(5): p. 664-+.
17. Zeng, X.Y., et al., *A New Transparent Conductor: Silver Nanowire Film Buried at the Surface of a Transparent Polymer.* Advanced Materials, 2010. **22**(40): p. 4484-4488.
18. Zhang, W., et al., *Analysis of the size effect in electroplated fine copper wires and a realistic assessment to model copper resistivity.* Journal of Applied Physics, 2007. **101**(6).
19. Marzi, G.D., et al., *Probing intrinsic transport properties of single metal nanowires: Direct-write contact formation using a focused ion beam.* Journal of Applied Physics, 2004. **96**(6): p. 3458-3462.

20. Bid, A., A. Bora, and A.K. Raychaudhuri, *Temperature dependence of the resistance of metallic nanowires of diameter >= 15 nm: Applicability of Bloch-Gruneisen theorem.* Physical Review B, 2006. **74**(3).
21. Karim, S., et al., *Investigation of size effects in the electrical resistivity of single electrochemically fabricated gold nanowires.* Physica E-Low-Dimensional Systems & Nanostructures, 2008. **40**(10): p. 3173-3178.
22. Ou, M.N., et al., *Electrical and thermal transport in single nickel nanowire.* Applied Physics Letters, 2008. **92**(6).
23. Volklein, F., et al., *The experimental investigation of thermal conductivity and the Wiedemann-Franz law for single metallic nanowires.* Nanotechnology, 2009. **20**(32).
24. Stojanovic, N., et al., *Direct measurement of thermal conductivity of aluminum nanowires.* Applied Physics Letters, 2009. **95**(9).
25. Rosenberg, H.M., *The solid state : an introduction to the physics of crystals for students of physics, materials science, and engineering*. Oxford physics series. 1975, Oxford Eng.: Clarendon Press. 234 p.
26. Lin, H., et al., *Thermal and Electrical Conduction in Ultrathin Metallic Films: 7 nm down to Sub-Nanometer Thickness.* Small, 2013. **9**(15): p. 2585-2594.
27. Ma, W.G. and X. Zhang, *Study of the thermal, electrical and thermoelectric properties of metallic nanofilms.* International Journal of Heat and Mass Transfer, 2013. **58**(1-2): p. 639-651.
28. Wilson, R.B. and D.G. Cahill, *Experimental Validation of the Interfacial Form of the Wiedemann-Franz Law.* Physical Review Letters, 2012. **108**(25).

29. Lin, H., et al., *Thermal and electrical conduction in 6.4 nm thin gold films.* Nanoscale, 2013. **5**(11): p. 4652-4656.

30. Reddy, N. and Y.Q. Yang, *Non-traditional lightweight polypropylene composites reinforced with milkweed floss.* Polymer International, 2010. **59**(7): p. 884-890.

31. Sakthivel, J.C., S. Mukhopadhyay, and N.K. Palanisamy, *Some studies on Mudar fibers.* Journal of industrial textiles, 2005. **35**(1): p. 14.

32. Shakyawar, D.B., R.S. Dagur, and N.P. Gupta, *Studies on milkweed fibres.* Indian Journal of Fibre & Textile Research, 1999. **24**(4): p. 264-268.

33. Crews, P.C., et al., *Evaluation of Milkweed Floss as an Insulative Fill Material.* Textile Research Journal, 1991. **61**(4): p. 203-210.

34. Drean, J.Y.F., et al., *Mechanical Characterization and Behavior in Spinning Processing of Milkweed Fibers.* Textile Research Journal, 1993. **63**(8): p. 443-450.

35. Louis, G.L. and B.A.K. Andrews, *Cotton Milkweed Blends - a Novel Textile Product.* Textile Research Journal, 1987. **57**(6): p. 339-345.

36. Cheng, Z., et al., *Electron Scattering across Grain Interface in sub-5 nm Extremely Confined Domains.* arXiv:1410.0737 [cond-mat.mes-hall], 2014.

37. Guo, J.Q., X.W. Wang, and T. Wang, *Thermal characterization of microscale conductive and nonconductive wires using transient electrothermal technique.* Journal of Applied Physics, 2007. **101**(6).

38. Feng, X.H. and X.W. Wang, *Thermophysical properties of free-standing micrometer-thick Poly (3-hexylthiophene) films.* Thin Solid Films, 2011. **519**(16): p. 5700-5705.

39. Liu, G., et al., *Characterization of Thermal Transport in One-dimensional Solid Materials.* Journal of Visualized Experiments, 2014. **83**.

40. McCrea, J.L., et al., *Electrical resistivity as a characterization tool for nanocrystalline metals.* Nanophase and Nanocomposite Materials Iii, 2000. **581**: p. 461-466.

41. Frobose, K. and J. Jackle, *On the temperature dependence of the electrical resistivity of amorphous metals.* Journal of Physics F: Metal Physics, 1977. **7**(11).

42. Nath, P. and K.L. Chopra, *Thermal-Conductivity of Copper-Films.* Thin Solid Films, 1974. **20**(1): p. 53-62.

43. Patterson, J. and B. Bailey, *Solid-State Physics: Introduction to the Theory, Second Edition.* Solid-State Physics: Introduction to the Theory, Second Edition, 2010: p. 1-827.

44. MEADEN, G., *Electrical resistance of metals(Book on theory and measuring techniques for electrical resistance of metals at low temperatures and cryogenics).* NEW YORK, PLENUM PRESS, 1965. 218 P, 1965.

45. Kittel, C., *Introduction to solid state physics*. 8 ed. 2005, Hoboken, NJ: J. Wiley.

46. Kim, S., H. Suhl, and I.K. Schuller, *Surface phonon scattering in the electrical resistivity on Co/Ni superlattices.* Physical Review Letters, 1997. **78**(2): p. 322-325.

47. Kastle, G., et al., *Size effect of the resistivity of thin epitaxial gold films.* Physical Review B, 2004. **70**(16).

48. Ma, W.G., X. Zhang, and K. Takahashi, *Electrical properties and reduced Debye temperature of polycrystalline thin gold films.* Journal of Physics D-Applied Physics, 2010. **43**(46).

49. Cahn, R., P. Haasen, and E. Kramer, eds. *Materials Science and Technology*. ed. P.L. Rossiter and J. Bass. Vol. 3A. 1991, VCH: New York.

50. Mayadas, A.F. and M. Shatzkes, *Electrical-Resistivity Model for Polycrystalline Films - Case of Arbitrary Reflection at External Surfaces.* Physical Review B, 1970. **1**(4): p. 1382-&.

51. Mayadas, A.F., M. Shatzkes, and J.F. Janak, *Electrical Resistivity Model for Polycrystalline Films - Case of Specular Reflection at External Surfaces.* Applied Physics Letters, 1969. **14**(11): p. 345-&.

52. Samsonov, G.V., *Handbook of the physiochemical properties of elements.* 1968.

53. Zhang, Q.G., et al., *Influence of grain boundary scattering on the electrical and thermal conductivities of polycrystalline gold nanofilms.* Physical Review B, 2006. **74**(13).

54. Zhang, X., et al., *Thermal and electrical conductivity of a suspended platinum nanofilm.* Applied Physics Letters, 2005. **86**(17).

55. Lu, Y.Z., et al., *Close correlation between transport properties and glass-forming ability of an FeCoCrMoCBY alloy system.* Intermetallics, 2012. **30**: p. 144-147.

56. Andersen, O.K. and Mackinto.Ar, *Fermi Surfaces and Effective Masses in Fcc Transition Metals.* Solid State Communications, 1968. **6**(5): p. 285-&.

57. Nagel, S.R., *Temperature dependence of the resistivity in metallic glasses.* Physical Review B, 1977. **16**(4).

58. Tsuei, C.C., *Anomalous Electrical-Conduction in Disordered and Non-Crystalline Metallic Conductors.* Solid State Communications, 1978. **27**(7): p. 691-695.

59. Ziman, J.M., *Electrons and phonons: the theory of transport phenomena in solids*. 2001: Oxford University Press.

60. Zhang, Y., et al., *Determining the Wiedemann-Franz ratio from the thermal Hall conductivity: Application to Cu and YBa2Cu3O6.95.* Physical Review Letters, 2000. **84**(10): p. 2219-2222.

61. Lin, H., et al., *Electron Transport and Bulk-like Behavior of Wiedemann-Franz Law for Sub-7 nm-thin Iridium Films on Silkworm Silk.* ACS applied materials & interfaces, 2014.

62. Singh, A., S. Hede, and M. Sastry, *Spider silk as an active scaffold in the assembly of gold nanoparticles and application of the gold–silk bioconjugate in vapor sensing.* Small, 2007. **3**(3): p. 466-473.

63. Steven, E., et al., *Carbon nanotubes on a spider silk scaffold.* Nature communications, 2013. **4**.

64. Amdursky, N., et al., *Electronic Transport via Proteins.* Advanced Materials, 2014.

65. Timalsina, Y.P., et al., *Effects of nanoscale surface roughness on the resistivity of ultrathin epitaxial copper films.* Nanotechnology, 2015. **26**(7): p. 075704.

66. Kojda, D., et al., *Temperature-Dependent Thermoelectric Properties of Individual Silver Nanowires.* arXiv preprint arXiv:1410.1467, 2014.

67. Cheng, Z., et al., *Electron Scattering across Grain Interface in sub-5 nm Extremely Confined Domains.* arXiv preprint arXiv:1410.0737, 2014.

68. Cheng, Z., et al., *Phonon Softening and Weak Temperature-dependent Lorenz Number for Bio-supported Ultra-thin Ir Film.* arXiv preprint arXiv:1410.1912, 2014.

69. Bayle, M., et al., *Experimental investigation of the vibrational density of states and electronic excitations in metallic nanocrystals.* Physical Review B, 2014. **89**(19).

70. Ghosh, S.K., *Kubo gap as a factor governing the emergence of new physicochemical characteristics of the small metallic particulates.* Assam University Journal of Science and Technology, 2011. **7**(2): p. 114-121.

71. Smith, D.R. and F.R. Fickett, *Low-Temperature Properties of Silver.* Journal of Research of the National Institute of Standards and Technology, 1995. **100**(2): p. 119-171.

72. Bifano, M.F.P., et al., *Effects of heat treatment and contact resistance on the thermal conductivity of individual multiwalled carbon nanotubes using a Wollaston wire thermal probe.* Journal of Applied Physics, 2012. **111**(5).